ORIGINAL ARTICLE

lajss.org Latin American Journal of Solids and Structures

www.lajss.org

Numerical Analysis of the Seismic Performance of Rigid Beam-To-Column Moment Connections Equipped with Steel Slit Damper (SSD)

Mahdi Hosseini[a]*, Li Haitao[a]*, Ileana Corbi[b], Ottavia Corbi[b]

[a*] Department of Building Engineering, College of Civil Engineering, Nanjing Forestry University, Nanjing, Jiangsu 210037, China.
E-mails: mahdi.struct@njfu.edu.cn, lhaitao1982@126.com
[b] Dipartimento di Strutture per l'Ingegneria e l'Architettura, Università degli Studi di Napoli Federico II, Napoli 80138, Italy.
E-mails: ileana.corbi@unina.it, ottavia.corbi@unina.it

*Corresponding author.

https://doi.org/10.1590/1679-78256994

Abstract:
In the present research, the finite-element method (FEM) implemented in the ABAQUS software is used to evaluate several numerical models. This study presents a composite system of slit dampers coupled with column-attached seats, where excessive loading of the structural system leads to the yielding of the slit damper rather than damaging main structural elements, especially the beams. In this respect, four aspects of the behavior of such connections are herein investigated to come up with an in-depth insight; these include aspect ratio, distance ratio, compactness ratio, and thickness ratio. Variations of the mentioned ratios are explained and compared by assigning differences that can be applied based on the connection rotation hysteresis curve, displacement envelope curve, dissipated energy, plastic strain, and stress contour. According to the results of these studies, it was figured out that an increase in aspect ratio, a decrease in distance ratio, and/or a change in thickness ratio tend to lower the performance of a slit damper.

Keywords:
steel slit damper (SSD); finite-element analysis on ABAQUS; split-T seat; cyclic loading

Graphical abstract

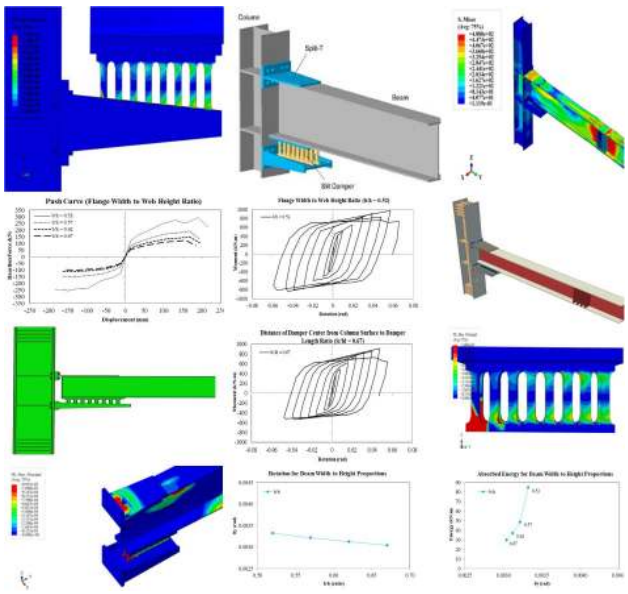

Received February 14, 2022. In revised form February 17, 2022. Accepted February 17, 2022. Available online February 21, 2022
https://doi.org/10.1590/1679-78256994

Latin American Journal of Solids and Structures. ISSN 1679-7825. Copyright ©2021. This is an Open Access article distributed under the terms of the Creative Commons Attribution License, which permits unrestricted use, distribution, and reproduction in any medium, provided the original work is properly cited.

1. Introduction

A very common event upon which a structure fails under seismic loading is the failure of the beam-column connection. Such a failure leads to the loss of the structural strength and hence triggers the collapse of different stories. Prior to the occurrence of the great earthquake events in the Northridge (USA, 1994) and Kobe (Japan, 1995), deployment of special moment frames with welded beam-column connections was a pretty common approach to seismic-resistant design of structures because of its economic benefits and the large plastic deformability of such connections (Miller 1998; Park H. et al., 2020). After the mentioned earthquake events, however, as researchers observed widespread cracks in the mentioned connections, they figured out that the previous perceptions were largely unrealistic (Sofias C.E. et al., 2015). Indeed, the Northridge earthquake indicated that the use of special moment frames with completely welded beam-column joints cannot prevent brittle failure of the connection in a steel structure even if all technical requirements are carefully observed in the design and construction phases. This was caused due to lack of flexibility in rigid beam-column joints of the steel moment frames, which led to brittle failure and unexpected cracks in these joints (Oh S.H et al., 2005). In many cases, sudden failure of the beam had prevented the formation of a plastic joint at the column face. In this respect, several solutions were proposed to move the plastic joint kind of farther from the column face (Kobori T et al., 1992). Some of these solutions included the use of mechanical energy-dissipating devices into the connections to make them able to tolerate large earthquake events. Examples of such energy-dissipating systems include metallic dampers such as TADAS (Tsai K. et al., 1993),honey-comb dampers (Koken A. et al., 2011), buckling-restrained brace (BRB) (Iwata M. et al., 2003; Sabelli R., et al., 2003; Iwata, M., et al., 2006; Tremblay R. et al., 2006), and slit dampers (Benavent Climent et al., 1998; Lee, M.H. et al., 2002; Benavent Climent, 2006; Chan, R. et al., 2008). For the most part, these devices are designed in the form of attached elements in the bracing system to a frame structure. Other elements were developed to serve as reinforcement to the beam-column joints in a frame structure, with them attached to lateral load-bearing system of the structure (*e.g.*, bracing system) (Koetake, Y. et al., 2005; Oh S. et al., 2006; Inoue K. et al., 2006). In the present research, steel slit damper (SSD) is used as a damper element for vertical loads applied to beam-column connections in a moment frame. An SSD is composed of a plate with several slits of predefined length. It is usually installed near the beam-column connection and is deformed under the effect of relatively small movements between its supporting flanges (Oh, S.H. et al., 2005). In such a structural system, vertical load-bearing beams are set on the mentioned dampers and column-attached plates host the damper in the vicinity of the load-bearing column (Tagawa H.et al., 2016). In this way, energy is dissipated and plastic deformations occur to the damper to prevent possible damages to the main structural members (Oh S.H et al., 2005). Lee et al. (2002) investigated the performance of a proposed beam connection where SSD was used as an energy absorber device. Test results and numerical analysis showed that the response of the structure equipped with the proposed connection was in agreement with the predicted outcomes in terms of structural strength and stiffness. When the damper strength was designed to be smaller than the beam, the connection rotation-induced deformation was focused on the damper due to the instantaneous declination of the moment-resisting members. With increasing the damper/beam strength ratio and/or the rotation angle, the beam had its flexibility improved gradually (Chan R. et al., 2008). Based on a set of numerical simulations and laboratory experiments, Hedayat (2015) predicted the failure point of unbuckled SSDs based on cumulative plastic strain. They figured out that, compared to other dampers, these dampers offer much longer failure times thanks to their large energy absorption capabilities (Hedayat A.A., 2015).Installation of an SSD into a structure and the geometry of its different elements must be in such a way to ensure that the damper will be deformed and rather flow under the effect of shear, bending, or axial loads that cause relative displacement of the story due to the lateral load. Otherwise, the damper will not work to dissipate energy (Ahmadie Amiri et al., 2018; Kiani et al., 2020). In their research, Oh et al. (2009) proposed an SSD-reinforced connection to address the problem of seismically weak beam-column connection in steel moment frames. Results of the tests performed by these researchers indicated improved hysteresis behavior of the SSD-reinforced connection. Their findings further showed that the energy dissipation and plastic deformation were favorably concentrated on the SSD, thereby preventing inelastic deformation of the beam and column across the system (Kiani et al., 2020). Performing a parametric study on the geometry of SSD-reinforced connections in a moment frame through finite-element method (FEM), Saffari et al. (2013) proposed optimal design parameters for increasing the formability of such connections (Saffari H. et al., 2013). Recent studies have shown that the incorporation of SSD into moment frames can address many drawbacks of common connections in the steel frames. For instance, an SSD-reinforced steel frame exhibits improved flexibility and the SSD creates a plastic joint at the beam section, thereby absorbing a large amount of energy that is later on dissipated through structural oscillations and plastic joints. Koken et al. (2011) presented an experimental study where they investigated the performance of three connections, namely normal connection, reinforced connection, and SSD-incorporated connection. Based on the results, they figured out that plastic deformations are fully absorbed by the damper in the latter system, with the connection being repairable after the

earthquake (Koken A. et al., 2011). Two of the most remarkable features of an SSD-incorporated connection include the elimination of shear load to the beam flange within the connection zone and a shift of the plastic joint into the beam at a position far from the connection (Okada K. et al., 2001). In such a system, one must consider the operational constraints when designing the connections and proposing their optimal geometry (Engelhardt M. D. et al., 1998).

The present research is aimed at parametric investigation of a composite connection system including SSD and column-attached seats based on the study by (Oh et al., 2009). The objective is to have the SSD yielded as the applied load to the structural system increases abruptly to prevent any damage to the main structural members, especially the beams. Accordingly, FEM-based modeling in the ABAQUS software was used to evaluate the behavior of connections across a specific steel moment frame equipped with SSD. In this respect, we analyzed the effects of four components affecting the behavior of the mentioned connections.

2. Materials and methods

2.1. Structural configuration of the proposed beam to column connection

A favorable approach to structural design for controlling the damage in a moment frame system is the fabrication of replaceable elements and limiting the damage through an energy absorption system based on yielding members attached to the main load-bearing members and then replacing them upon guided damages (Engelhardt M. D. et al., 1998). In this approach, the dampers on which the damage is concentrated are attached to the main frame by means of replaceable bolted joints, so that beam and columns can be easily repaired as the damage is guided toward the mentioned dampers (Uang C. M. et al., 1998). Due to their remarkable stiffness and easy fabrication, SSDs have been acknowledged as a good method of increasing the structural performance by triggering local buckling and absorbing the energy excreted by lateral loads through the aforementioned mechanism. Figure 1 presents a demonstration of an SSD and the way it is attached to the structure (adopted from Oh et al. (2009)). This SSD is the basis of the numerical simulations performed in the present work.

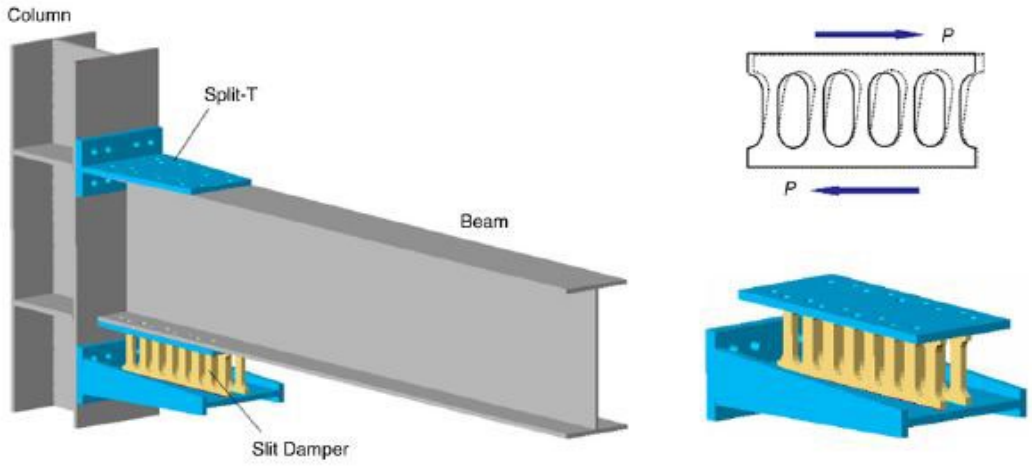

Figure 1. Details of the proposed beam to column connection equipped with an SSD, as proposed by (Oh et al., 2009).

The proposed system uses the connection between the column flange and the top flange of the beam as a mean to transfer gravitational loads from the beams to the columns. Moreover, one can retain the split-T at the top flange within its elastic zone to keep the center of rotation within the top flange of the beams. In order to limit the damage to the connection element without damaging the main structural elements, it is necessary for the connection to have a relatively high stiffness and to yield before the main structural members. In an SSD, energy dissipation occurs through plastic deformation of the vertical supports. SSDs offer very good energy dissipation capacities coupled with high stiffness levels, making them a good candidate for being used as a connection element in the proposed system in this study. In order to predict the yield strength and deformation at yield of the SSD, the damper supports were idealized and the round ends of the supports were assumed to be perfectly straight. Figure 2 presents details of the simplifications proposed by (Oh et al., 2009). Based on these simplifications, one can extract the yield strength and maximum apparent strength of the SSD analytically. Figure 3 shows the analytic model as well as shear-bending axes of the proposed

connection. Equations (1) to (3) express formulations for idealizing the SSD and calculating its yield strength and ultimate strength, respectively.

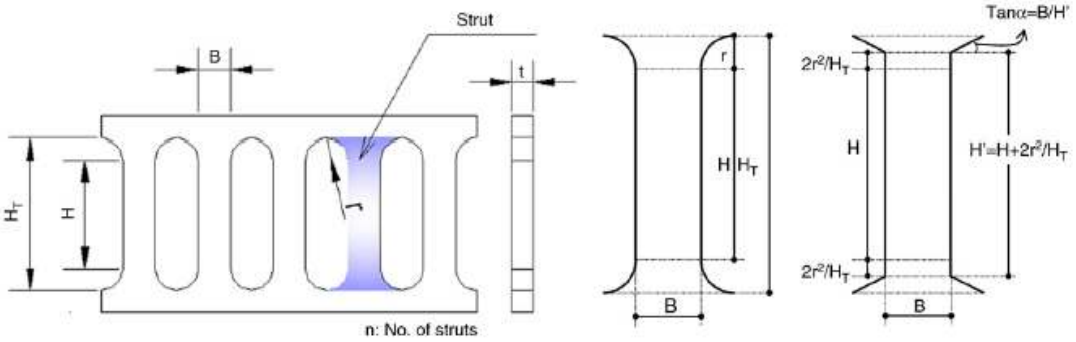

Figure 2. Idealization of the proposed SSD (Oh et al., 2009).

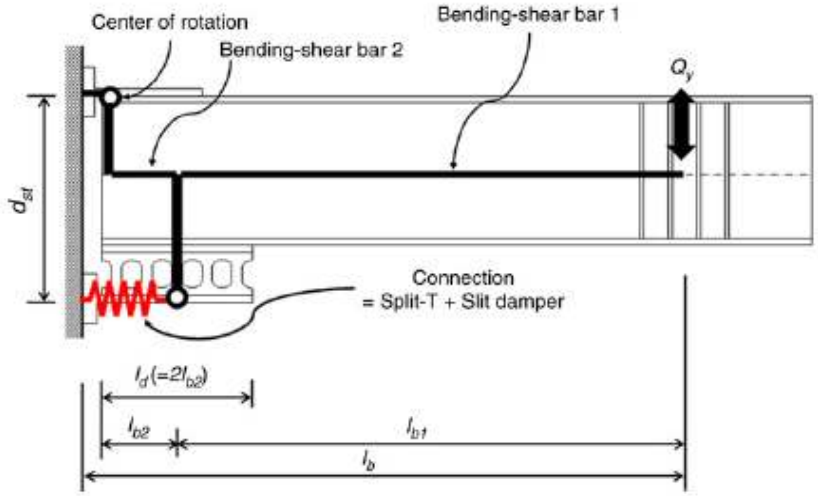

Figure 3. Analytic model of the connection, center of rotation, and shear-bending axes of the evaluated system (Oh et al., 2009)

$$H' = H + \frac{2r^2}{H_T} \tag{1}$$

$$P_y = min\left\{n\frac{\sigma_y t B^2}{2H'}, n\frac{2\sigma_y t B}{3\sqrt{3}}\right\} \tag{2}$$

$$P_u = min\left\{n\frac{\sigma_u t B^2}{2H'}, n\frac{2\sigma_u t B}{3\sqrt{3}}\right\} \tag{3}$$

In Equation (1), H' is the equivalent height, H is the slit height excluding the curvature, H_T is total slit height, and r is the slit radius in the curvature zone. In Equations (2) and (3), n is the number of vertical supports, t is the plate thickness, P_y is the yield strength, P_u is the ultimate strength, σ_y is the yield stress, σ_u is the ultimate stress, and B is the support width. The $\frac{2}{3}$ coefficient in the second part of Equations (2) and (3) indicates that, within the elastic region, the ratio of average shear stress to maximum shear stress would be equal to $\frac{2}{3}$ as long as the $\frac{B}{H}$ shape factor remains below 1. Displacement at yield of the SSD (δ_y) can be obtained from Equation (4), which expresses a simplified analytic approach:

$$\delta_y = \frac{1.5P_y H_T}{nEtB}\left[\left(\frac{H'}{B}\right)^2 + 2.6\right] \tag{4}$$

where E is the elasticity modulus of the SSD material. In case of using split-T seats (with their details, simplifications, and deformation scheme are demonstrated in Figure 4) and then completing the connection with an SSD, one may describe initial connection stiffness with the help of Equation (5).

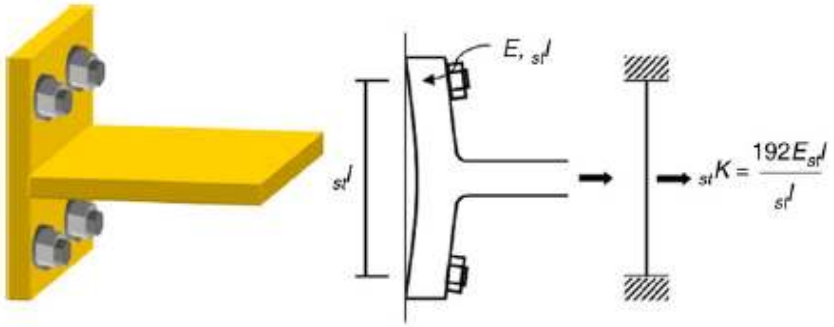

Figure 4. Details, simplifications, and deformation scheme of split-T seat (Oh et al., 2009).

$$K^{-1} = {}_{b1}K^{-1} + {}_{b2}K^{-1} + {}_{con}K^{-1} \tag{5}$$

in which K^{-1} is the initial connection stiffness, ${}_{b1}K$ is the initial stiffness corresponding to the beam shear force due to the end displacement of the beam along the shear-bending axis 1, ${}_{b2}K$ is the initial stiffness corresponding to the beam shear force due to the end displacement of the beam along the shear-bending axis 2, and ${}_{con}K$ is the initial stiffness corresponding to the composite connection including split-T seats and SSD. By applying the principle of virtual work, one can evaluate the mentioned stiffness values by means of Equations (6) to (11).

$${}_{b1}K^{-1} = \frac{l_{b1}^3}{3E_{b1}I} + \frac{l_{b1}}{{}_{\omega}AG} \tag{6}$$

$${}_{b2}K^{-1} = \frac{l_{b2}(l_{b1}^2 + l_{b1}l_{b2} + l_{b2}^2)}{3E_{b2}I} + \frac{2l_{b1}}{{}_{\omega}AG} \tag{7}$$

$${}_{con}K^{-1} = {}_{con}k^{-1}\left(\frac{l_b}{d_{st}}\right)^2 \tag{8}$$

$${}_{con}k^{-1} = {}_{st}K^{-1} + {}_{d}K^{-1} \tag{9}$$

$${}_{st}K = \frac{192E_{st}I}{{}_{st}l} + \frac{2l_{b1}}{{}_{\omega}AG} \tag{10}$$

$${}_{d}K = \frac{P_y}{\delta_y} \tag{11}$$

In the above equations, l_{b1} and l_{b2} denote the lengths of the shear-bending axes 1 and 2, respectively, I_{b1} and I_{b2} are effective moment of inertial along the shear-bending axes 1 (for which only the beam web exhibits an effective moment) and 2 (for which the upper part of the beam has an effective moment), respectively, ${}_{\omega}A$ is the cross-sectional area of the beam web, ${}_{st}l$ is the split-T flange width, ${}_{st}K$ is the lateral stiffness of the split-T seat, ${}_{d}K$ is the lateral stiffness of the SSD, δ_y is the displacement at yield of the SSD, and G is the shear modulus. Accordingly, theoretical shear force of the beam (Q_y) and bending moment at the column surface (M_y) for an SSD in full plastic mode can be obtained from Equations (12) and (13), respectively.

$$Q_y = \frac{P_y a_{st}}{l_{b1}} \tag{12}$$

$$M_y = Q_y l_b = \frac{P_y d_{st} l_b}{l_{b1}} \tag{13}$$

In an ultimate case, the shear force of the beam (Q_u) and bending moment at the column surface (M_u) corresponding to the maximum strength of the SSD can be obtained from Equations (14) and (15), respectively.

$$Q_u = \frac{P_u a_{st}}{l_{b1}} \tag{14}$$

$$M_u = Q_u l_b = \frac{P_u d_{st} l_b}{l_{b1}} \tag{15}$$

2.2. Validation

In order to ensure the validity of the modeling as a first step, a numerical model was developed using FEM in ABAQUS based on the design principles for SSDs presented by Oh et al. (2009). Figures 5 and 6 present experimental setup and details of the numerical and experimental model D1 according to Oh et al. (2009). This model (*i.e.*, D1) has been frequently used for validation purposes in different research works. In this model, geometrical symmetry is utilized to downscale the dimensions of the numerical and experimental models. Hence, the experimental setup was configured into the form an external T-like system.

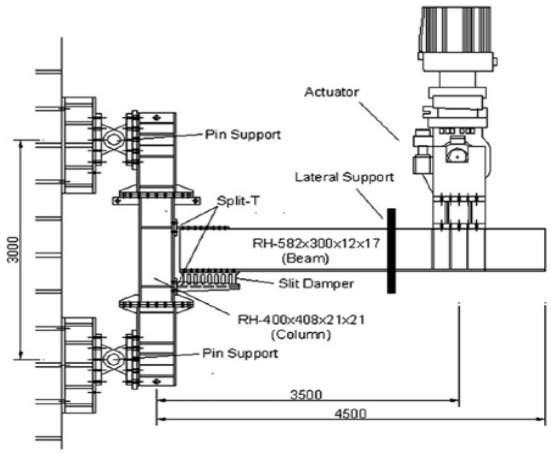

Figure 5. Setup of the experimental model (Oh et al., 2009).

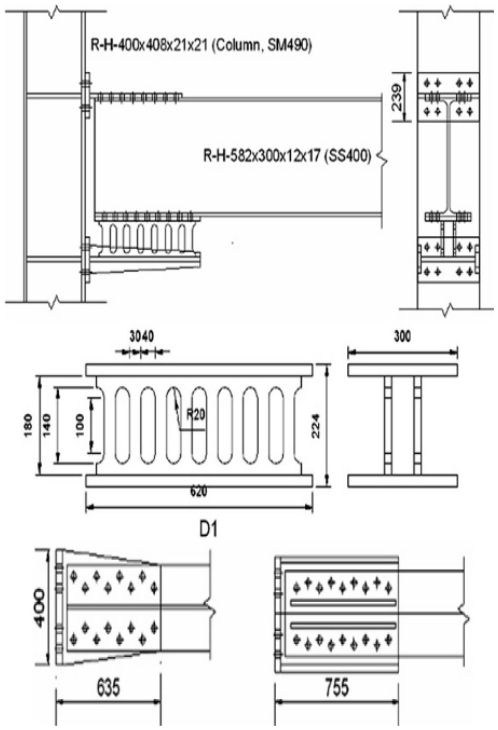

Figure 6. Details of connections, cross-sectional characteristics, and model geometry (Oh et al., 2009).

In accordance with the details given in Figures 5 and 6, the studied beam and column had H-582×302×12×17 and H-400×400×21×21 wide-web sections, respectively. Table 1 presents characteristics of the beam and column in the studied model. Tables 2 and 3 further report characteristics of the split-T seats and SSD. The friction and tensile connections in the experimental samples were restrained by high-strength F10T bolts to provide them with high enough strength to avoid slippage or detachment at any time before the slit reaches its ultimate strength. The beam and column in the numerical and experimental models were made from KS SS400 and SM490 steel, respectively. The SSDs were also made from KS SS400 soft steel. Details of the used materials for building the validation model are presented in Table 4.

Table 1. Cross-sectional characteristics of the beam and column used in the numerical and experimental models (Oh et al., 2009).

Structural Elements			
	Element	**Unit**	**Magnitude**
Column H-400x400x21x21	h	mm	400
	b	mm	408
	t_f	mm	21
	t_w	mm	21
Beam H-582x300x12x17	h	mm	582
	b	mm	302
	t_f	mm	17
	t_w	mm	12

Table 2. Cross-sectional properties of the base seat and top split-T separator (Oh et al., 2009).

Split-T			
	Element	**Unit**	**Magnitude**
Upper Section	l_u	mm	635
	h_u	mm	239
	w_u	mm	300~400
	t_{uf}	mm	35
	t_{uw}	mm	22
Lower Section	l_l	mm	755
	h_l	mm	239
	w_l	mm	400
	t_{lf}	mm	35
	t_{lw}	mm	22

Table 3. Characteristics of the SSD (Oh et al., 2009).

Slit Damper		
Element	**Unit**	**Magnitude**
D1	mm	620
T	mm	32
W	mm	300
H_A	mm	224
H_T	mm	140
H	mm	100
B	mm	30
r	mm	20
t	mm	19
n	No.	16

Table 4. Mechanical properties of the materials used in the validation phase.

Material	*Section*	*Yield Strength*	*Ultimate Strength*	*Elongation*	*Reduction Area*
		Mpa	**Mpa**	**%**	**%**
KS SS400	Beam Web	339	488	27	70
	Beam Flange	318	480	30	67
	Slit Damper	208	464	30	63
SM490	Column Web	395	554	27	74
	Column Flange	378	551	24	71
	Split-T Web	388	577	25	71
	Split-T Flange	386	573	24	69
F10T	Bolt	900	1000	14	40

In the present research, the loading scheme was based on the rotation around the hinge formed in the top split-T separator as measured in multiples of the yield rotation ratios per different loading cycles. The yield rotation is obtained by dividing the displacement at yield of the beam end by effective beam length. Figure 7 presents the loading scheme based on a multiple of the rotation of the top hinge, with different stages of the cyclic loading further indicated.

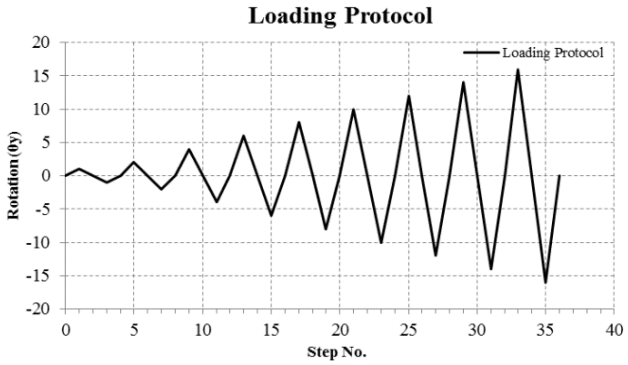

Figure 7. Modeling scheme for the validation model based on multiples of the yield rotation and different stages of cyclic loading.

Since a numerical model cannot handle a loading scheme with ambiguous coefficients, in the validation stage, we formulated this scheme based on the ratio of ultimate displacement at the end of the beam and virtually scaled time (Figure 8). This loading scheme, which was converted to an understandable format for the ABAQUS by changing the components of the original loading scheme presented in Figure 7, was also used in the numerical models that were developed based on the validation model. It is worth noting that the defined loading scheme is unique for each specific model with its particular geometrical-mechanical characteristics (*i.e.*, a different loading scheme was considered for each specific model). Table 5 lists the mechanical and geometrical characteristics of the validation model based on the definitions presented in the previous section. These are herein categorized under geometrical properties, mechanical properties, and load-bearing capacity. The geometry and meshing scheme of the validation model in the ABAQUS are demonstrated in Figure 9.

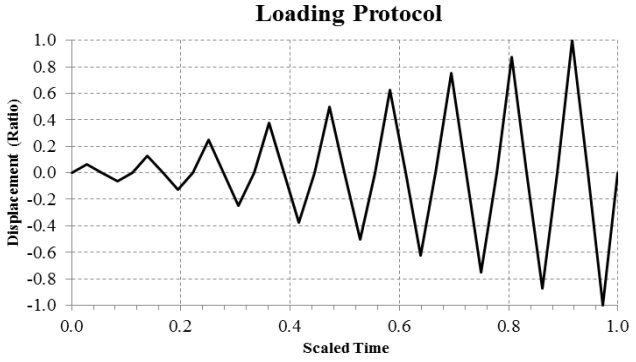

Figure 8. Loading scheme of the validation model based on the ultimate displacement ratio and scaled virtual time.

Table 5. Characteristics of the validation model.

Geometrical Properties			*Mechanical Properties*			*Load-bearing Capacity*		
σ_y	Mpa	208	l_b	mm	3300	Q_y	N	76931
σ_u	Mpa	464	l_d	mm	620	M_y	N.mm	2.54E+08
H_T	mm	140	l_{b2}	mm	310	Q_u	N	171615
H	mm	100	l_{b1}	mm	2855	M_u	N.mm	5.66E+08
B	mm	30	l_{st}	mm	130.5	θ_y	rad	0.003322
t	mm	19	d_{st}	mm	816			
r	mm	20	$_wA$	mm^2	6576			
n	No.	16	$_{b1}I$	mm^4	978835992			
H'	mm	105.7	$_{b2}\tilde{y}$	mm	225.5			
P_y	N	269163	$_{b2}I$	mm^4	63015977			
P_u	N	600441	$_{st}I$	mm^4	1429167			
δ_y	mm	0.443	$_{b1}K^{-1}$	mm/N	0.000043			
			$_{b2}K^{-1}$	mm/N	0.000072			
			$_{con}K^{-1}$	mm/N	0.000027			
			$_{st}k^{-1}$	mm/N	2,26E-07			
			$_{d}k^{-1}$	mm/N	1,65E-01			
			$_{con}k^{-1}$	mm/N	1,65E-01			
			K^{-1}	mm/N	0.000143			

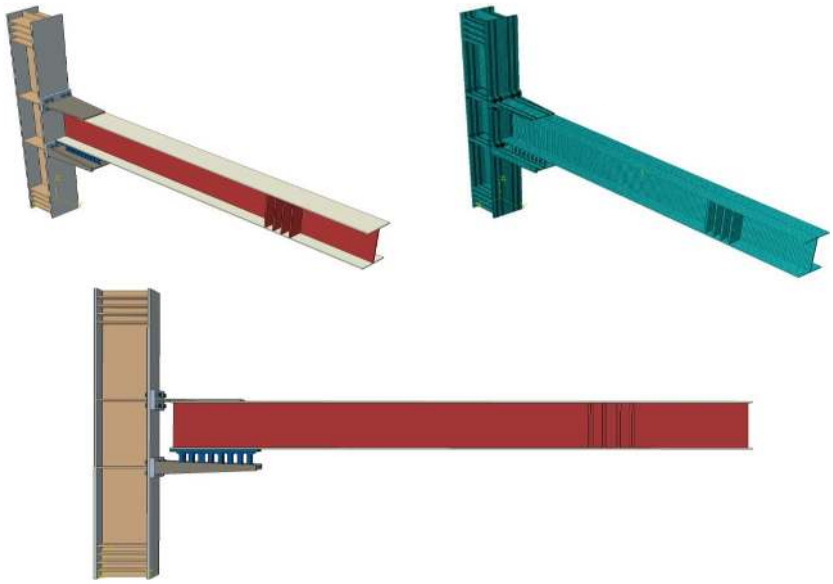

Figure 9. Geometry and meshing scheme of the numerical model developed in the ABAQUS.

In the numerical model, mesh size of different elements ranged from 5 to 20 mm depending on the element type. The elements were meshed with cubic 3D 8-noded grids with reduced integration (C3D8R). In order to prevent yielding and inappropriate deformations at the point of loading, the Hourglass upgraded control system was adopted. The welded connections of the beam to the SSD and top separator and the SSD to the base seat (as defined in Oh et al., (2009)) were modeled using tie mechanism. In the numerical model, connection of split-T plates to column was simulated using a high-strength bearing-friction bolted joint with the help of Hard Contact mechanism at the bolts, and friction mechanism, with a friction coefficient of 0.7, for the contact between the split-T steel plates and flange face of the column. The material behavior was supposed to be bilinear (elastic until the yield point and then plastic until the ultimate stress), with the details presented in Table 4. According to Oh et al. (2009), given the presence of lateral bearing, a lateral support was defined at a distance of 1 m from the vertical loading axis to control the out-of-plane behavior of the model and hence prevent the buckling of the beam web. Considering the cyclic loading scheme, the hysteresis curve presented by Oh et al. (2009) was compared to the results of numerical studies by the ABAQUS in the present research. Figure 10 compares the hysteresis curves of the reference model (Oh et al., 2009) and the numerical model.

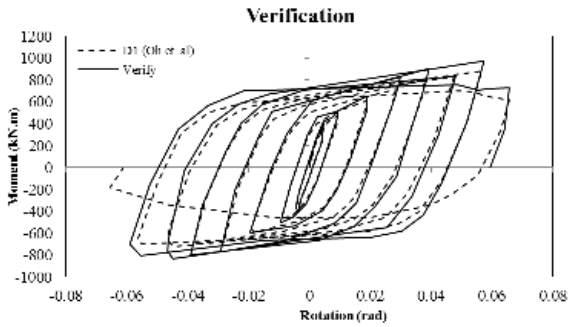

Figure 10. A comparison between hysteresis curves developed upon experimental investigations (Oh et al., 2009) and the numerical model built in the ABAQUS.

The comparison between the numerical model and experimental results indicates a good agreement between the two. Due to lack of information about post-damage behavior of the materials used in the experimental study (at least not clearly indicated in the relevant research), it was impossible to model the final segment of the hysteresis curve for the numerical model as it would call for extremely huge volumes of computation. On the hysteresis plots, the numerical model exhibited some 13.96% higher values in early cycles and some 11.06% higher values in the late cycles, as compared to the results of experimentations. Figures 11 and 12 compare plastic strain of the SSD between the experimental and the present numerical studies, with the details of stress and strain in other members of the studied numerical model further presented. Although the column-attached plates are not yielded, plastic strain of the top attachment plate and the beam web in the vicinity of the column indicate the occurrence of damage to the studied model. Considering the numerical and experimental results, it is evident that the yielding and plastic strain occurred to top and base parts of the SSD supports, especially for the supports that were farther from the column face, because of sequential distribution of stiffness and absorption of larger energies at the supports that are closer to the point of loading. Since the results of the validation model were acceptable, one needed to evaluate the composite connection with SSDs and split-T seats under a different set of conditions from the present status. A discussion on such an evaluation is presented in the following.

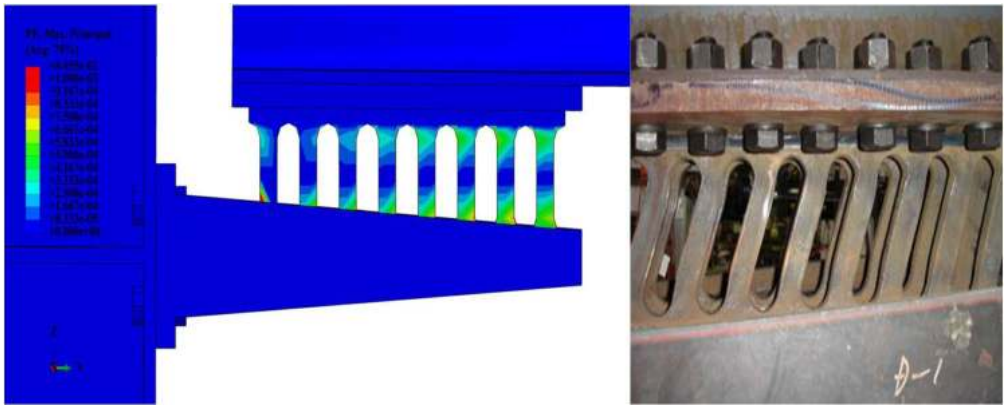

Figure 11. Comparison between plastic strain of the validation numerical model and plastic deformation of the experimental model.

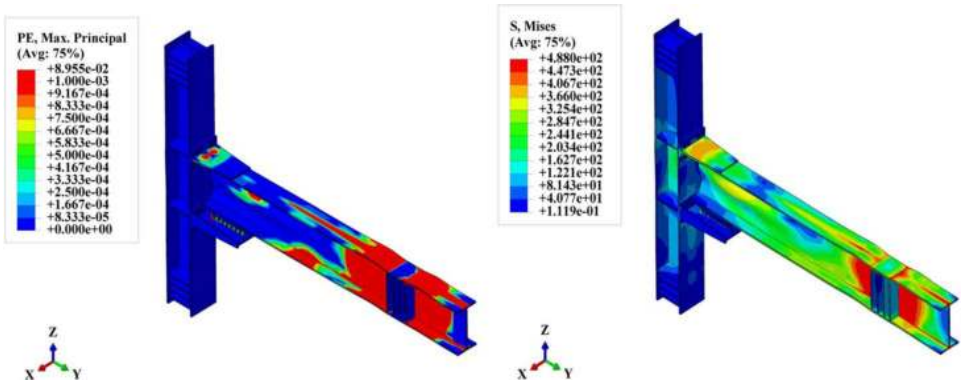

Figure 12. Contours of plastic strain and strain for the validation model in the final stage of loading.

2.3. Characteristic of the selected models

Following with this research, we evaluated the main components of the connection including the SSD by applying changes to the components affecting the behavior of the load-bearing system of the structure. The aspect ratio (beam web to height ratio) of the validation model was 0.52 and desirable performance was reported for this aspect ratio by Oh et al. (2009). A change in this aspect ratio can demonstrate the behavior of the structure with such beam-column connections at different ratios. A change in the ratio of distance from the center of area of the SSD to the column face to the SSD length, which is known to affect the stiffness of the connections of the seat plate and top separator to the column, is another factor affecting the behavior of the mentioned connections. This latter ratio for the validation model was 0.72. Similarly, the ratios of SSD base plate thickness to beam flange thickness (equal to 1.12 in the validation model) and also the base width to total width of the base and SSD (equal to 0.43 in the validation model) are among other factors affecting the behavior of the considered connections. In addition, one may refer to the material, number of slits, and slit height-to-width ratio as other factors affecting the behavior of composite connections including SSD and split-T seats. Acknowledging their paramount importance, the following four factors were considered in the present study: (1) flange width to beam height ratio, (2) SSD center to column face distance, (3) SSD base plate thickness to beam flange thickness ratio, and (4) ratio of SSD base width to total width of the base and SSD. Table 6 reports characteristics of the selected numerical models. Table 7 presents geometrical properties, displacement at yield, load-bearing capacity at yield, and ultimate load-bearing capacity of the SSD. Table 8 provides mechanical properties and stiffness of different components of the connection separately while reporting the ultimate stiffness of the connection in the numerical models studied in this work. Yield and ultimate shear and bending load-bearing capacities of the connection and bending moment-induced rotation at yield at the plastic hinge of the top separator of the studied numerical models are separately presented in Table 9.

Table 6. characteristics of the numerical models studied in this research.

Subject	Constant Case		Variable Case		Ratio	Model Name
	Name	Value	Name	Value		
Beam Aspect Ratio	Beam Height	582	Beam Flange Width	300	0.52	**BA_bh_52**
				330	0.57	**BA_bh_57**
				360	0.62	**BA_bh_62**
				390	0.67	**BA_bh_67**
Damper Distance Ratio	Damper Length	620	Axis Distance to the Column	385	0.62	**DD_cd_62**
				415	0.67	**DD_cd_67**
				445	0.72	**DD_cd_72**
Damper Aggregation Ratio	Strut+Void Width	70	Strut Width	24	0.34	**DA_BL_34**
				30	0.43	**DA_BL_43**
				36	0.51	**DA_BL_51**
Damper Thickness Ratio	Beam Flange Thickness	17	Damper Thickness	17	1	**DT_ttf_100**
				19	1.12	**DT_ttf_112**
				21	1.24	**DT_ttf_124**

Table 7. Geometrical properties, displacement at yield, and yield and ultimate load-bearing capacities of the SSD.

Model Name	σ_y	σ_u	H_T	H	B	t	r	n	H'	P_y	P_u	δ_y
	Mpa	Mpa	mm	mm	mm	mm	mm	No.	mm	N	N	mm
BA_bh_52	208	464	140	100	30	19	20	16	105.7	269163	600441	0.443
BA_bh_57	208	464	140	100	30	19	20	16	105.7	269163	600441	0.443
BA_bh_62	208	464	140	100	30	19	20	16	105.7	269163	600441	0.443
BA_bh_67	208	464	140	100	30	19	20	16	105.7	269163	600441	0.443
DD_cd_62	208	464	140	100	30	19	20	16	105.7	269163	600441	0.443
DD_cd_67	208	464	140	100	30	19	20	16	105.7	269163	600441	0.443
DD_cd_72	208	464	140	100	30	19	20	16	105.7	269163	600441	0.443
DA_BL_34	208	464	140	94	24	19	23	16	101.6	179316	400013	0.504
DA_BL_43	208	464	140	100	30	19	20	16	105.7	269163	600441	0.443
DA_BL_51	208	464	140	106	36	19	17	16	110.1	372059	829978	0.407
DT_ttf_100	208	464	140	100	30	17	20	16	105.7	240830	537237	0.443
DT_ttf_112	208	464	140	100	30	19	20	16	105.7	269163	600441	0.443
DT_ttf_124	208	464	140	100	30	21	20	16	105.7	297496	663645	0.443

Table 8. Mechanical and stiffness properties of separate components of the connection and ultimate stiffness of the connection (to be continued).

Model Name	l_b	l_d	l_{b2}	l_{b1}	l_{st}	d_{st}	$_wA$	$_{b1}I$	$_{b2}\tilde{y}$	$_{b2}I$	$_{st}I$
	mm	mm	mm	mm	mm	mm	mm^2	mm^4	mm	mm^4	mm^4
BA_bh_52	3300	620	310	2855	130.5	816	6576	978835992	225.5	63015977	1429167
BA_bh_57	3300	620	310	2855	130.5	816	6576	1060262932	228.7	64592160	1429167
BA_bh_62	3300	620	310	2855	130.5	816	6576	1141689872	231.6	65998786	1429167
BA_bh_67	3300	620	310	2855	130.5	816	6576	1223116812	234.3	67262014	1429167
DD_cd_62	3240	620	310	2855	130.5	816	6576	978835992	225.5	63015977	1429167
DD_cd_67	3270	620	310	2855	130.5	816	6576	978835992	225.5	63015977	1429167
DD_cd_72	3300	620	310	2855	130.5	816	6576	978835992	225.5	63015977	1429167
DA_BL_34	3300	620	310	2855	130.5	816	6576	978835992	225.5	63015977	1429167
DA_BL_43	3300	620	310	2855	130.5	816	6576	978835992	225.5	63015977	1429167
DA_BL_51	3300	620	310	2855	130.5	816	6576	978835992	225.5	63015977	1429167
DT_ttf_100	3300	620	310	2855	130.5	816	6576	978835992	225.5	63015977	1429167
DT_ttf_112	3300	620	310	2855	130.5	816	6576	978835992	225.5	63015977	1429167
DT_ttf_124	3300	620	310	2855	130.5	816	6576	978835992	225.5	63015977	1429167

Model Name	$_{st}k^{-1}$	$_dk^{-1}$	$_{con}k^{-1}$	$_{b1}K^{-1}$	$_{b2}K^{-1}$	$_{con}K^{-1}$	K^{-1}
	mm/N	mm/N	mm/N	mm/N	mm/N	mm/N	mm/N
BA_bh_52	2,27E-09	1,65E-03	1,65E-03	0.000043	0.000072	0.000027	0.000143
BA_bh_57	2,27E-09	1,65E-03	1,65E-03	0.000040	0.000071	0.000027	0.000138
BA_bh_62	2,27E-09	1,65E-03	1,65E-03	0.000038	0.000069	0.000027	0.000134
BA_bh_67	2,27E-09	1,65E-03	1,65E-03	0.000036	0.000068	0.000027	0.000130
DD_cd_62	2,27E-09	1,65E-03	1,65E-03	0.000043	0.000072	0.000026	0.000142
DD_cd_67	2,27E-09	1,65E-03	1,65E-03	0.000043	0.000072	0.000026	0.000142
DD_cd_72	2,27E-09	1,65E-03	1,65E-03	0.000043	0.000072	0.000027	0.000143
DA_BL_34	2,27E-09	2,81E-03	2,81E-03	0.000043	0.000072	0.000046	0.000162
DA_BL_43	2,27E-09	1,65E-03	1,65E-03	0.000043	0.000072	0.000027	0.000143
DA_BL_51	2,27E-09	1,09E-03	1,09E-03	0.000043	0.000072	0.000018	0.000133
DT_ttf_100	2,27E-09	1.84E-06	1.84E-06	0.000043	0.000072	0.000030	0.000146
DT_ttf_112	2,27E-09	1,65E-03	1,65E-03	0.000043	0.000072	0.000027	0.000143
DT_ttf_124	2,27E-09	1.49E-06	1.49E-06	0.000043	0.000072	0.000024	0.000140

Table 9. Yield and ultimate shear and bending load-bearing capacities of the connection and bending moment-induced rotation at yield at the plastic hinge of the top separator of the beam-column connection.

Model Name	Q_y	M_y	Q_u	M_u	ϑ_y
	N	N.mm	N	N.mm	rad
BA_bh_52	76931	253871377	171615	566328456	0.003322
BA_bh_57	76931	253871377	171615	566328456	0.003214
BA_bh_62	76931	253871377	171615	566328456	0.003122
BA_bh_67	76931	253871377	171615	566328456	0.003042
DD_cd_62	76931	249255534	171615	556031575	0.003361
DD_cd_67	76931	251563455	171615	561180016	0.003341
DD_cd_72	76931	253871377	171615	566328456	0.003322
DA_BL_34	51251	169128547	114329	377286759	0.002509
DA_BL_43	76931	253871377	171615	566328456	0.003322
DA_BL_51	106340	350921442	237220	782824754	0.004301
DT_ttf_100	68833	227148074	153550	506714935	0.003039
DT_ttf_112	76931	253871377	171615	566328456	0.003322
DT_ttf_124	85029	280594680	189679	625941978	0.003606

3. Findings

According to what was mentioned so far, the present study aims at parametric evaluation of the behavior of SSD-equipped connections. For this purpose, we considered the effects of changes in four parameters on the behavior of the structural system, namely (1) flange width to beam height ratio, (2) SSD center to column face distance, (3) SSD base plate thickness to beam flange thickness ratio, and (4) ratio of SSD base width to total width of the base and SSD. Changes in the mentioned ratios are herein considered and compared by assigning applicable differences to the reference model (validation model) based on the hysteresis curve of the connection rotation, displacement envelop curve, dissipated energy, plastic strain, and stress contours. The material properties, loading scheme, and geometrical properties other than the variable property were kept the same as those in the validation model.

3.1. Beam aspect ratio

The beam flange to height ratio can change load-bearing capacity of different members and the beam-column connection stiffness, making it an effective factor on the studied connection behavior. In order to compare different models with different aspect ratios in terms of their connection behavior, we herein considered the hysteresis curve of the structure for rotation around the top corner of the beam-column connection, displacement and energy envelop curve, plastic strain, and ultimate strain. Figure 13 presents schematic view of the connection plates for different beam flange to height ratios corresponding to different models. The following subsections report details of the results upon changing the considered parameter.

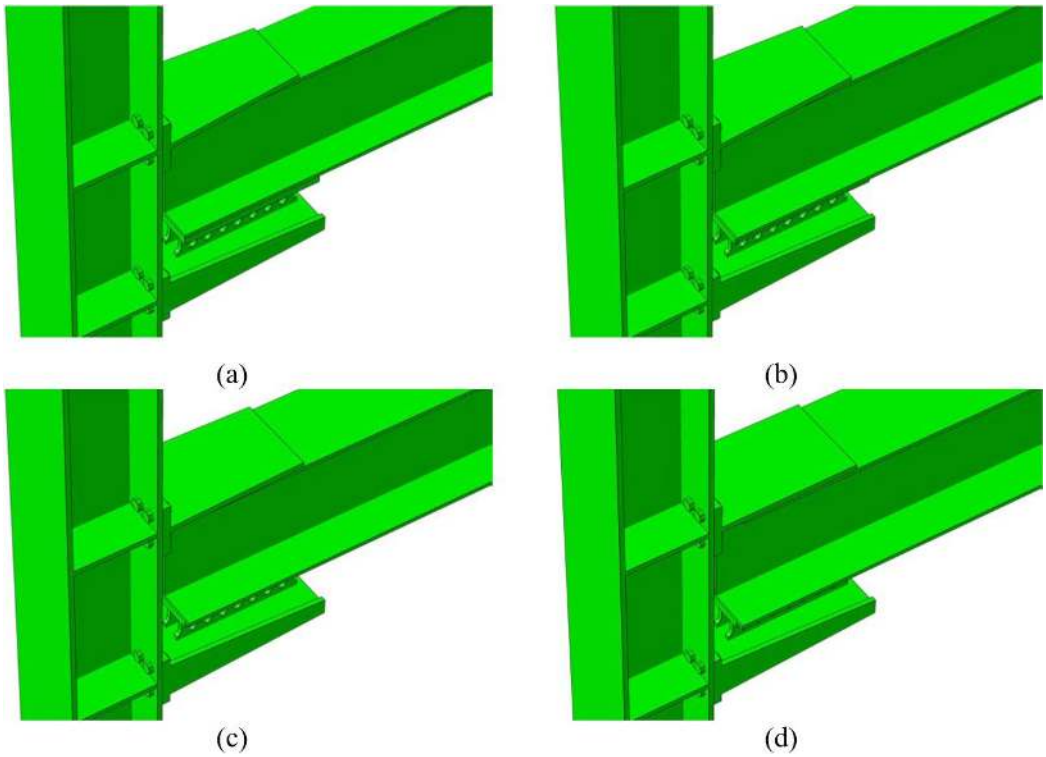

Figure 13. Schematic view of the connection of the beam flange to the connection plate and column for different samples with different aspect ratios: (a) BA_bh = 0.52, (b) BA_bh = 0.57, (c) BA_bh = 0.62, and (d) BA_bh = 0.67.

3.1.1. Connection rotation hysteresis curve

In order to evaluate the absorbed energy by a structure, one needs to extract hysteresis curves for cyclically loaded models. Accordingly, hysteresis curves of the studied models in this research were developed for different parameters, with each curve considering the effect of only one parameter. In this subsection, the results are presented for different beam flange to height ratios. Figure 14 presents the rotation-bending moment hysteresis curve considering the rotation hinge at the top corner of the beam-column connection plate in models of different aspect ratios. Knowing that the beam properties limited the changes in the flange width, the studied aspect ratios were limited in the range of 0.52 – 0.72. Evaluation of the hysteresis curve enables the selection of optimal aspect ratio or modification to the design philosophy to improve the states of other aspect ratios.

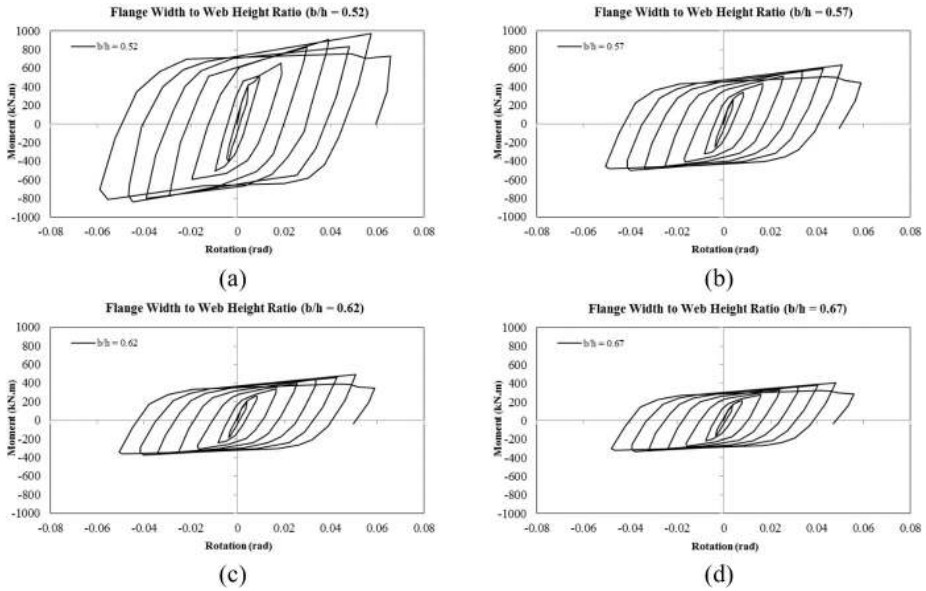

Figure 14. Rotation-bending moment hysteresis curve considering the rotation hinge at the top corner of the beam-column connection plate in models of different aspect ratios.

Considering the hysteresis curves presented in this subsection, it is evident that an increase in this aspect ratio narrows down the width of the hysteresis curve significantly. Such an increase further causes an insignificant reduction in the rotation of around the plastic hinge. The difference in ultimate rotation between the smallest and largest aspect ratios studied in this work was about 9.23%. Therefore, an increase in the aspect ratio tends to slenderize the hysteresis curves, insignificantly reduce the rotation capacity, and lower the load-bearing capacity and hence energy absorption capacity of the connection.

3.1.2. Displacement and energy envelop curves

In order to evaluate structural behavior of the models and extract support responses, one needs to develop envelop curves of the model capacities considering the corresponding hysteresis curves. A capacity curve can be obtained by extracting maximum load-bearing capacity and the corresponding displacement in each cycle along the hysteresis curve and increasing the applied cycling load until a point where the structure becomes unstable. The absorbed energy curve is developed by cumulatively summing up the area under the envelop curve. An increase in the energy absorption behavior of the system is expressed in the form of plastic strain and residual deformation. If a structural system fails to absorb the dynamic cyclic loads and convert them into potential energy (*i.e.*, plastic strain, residual deformation, etc.), this amount of energy will be released in the form of structural vibrations, elastic deformations, and heat, of which no evidence is expected on the hysteresis curve and the plot of stored energy. This subsection presents load-bearing capacity and energy envelop curves for different beam width to height ratios. Figure 15 shows the load– displacement envelop curve and cumulative energy for the beam-column connection at different aspect ratios. A comparison between different displacement envelop curves shows that an increase in the aspect ratio tends to lower the energy absorption and load-bearing capacity of the connection. In particular, ultimate strength decreased by 39% and 61% as the aspect ratio increased from 0.52 to 0.57 and 0.72, respectively.

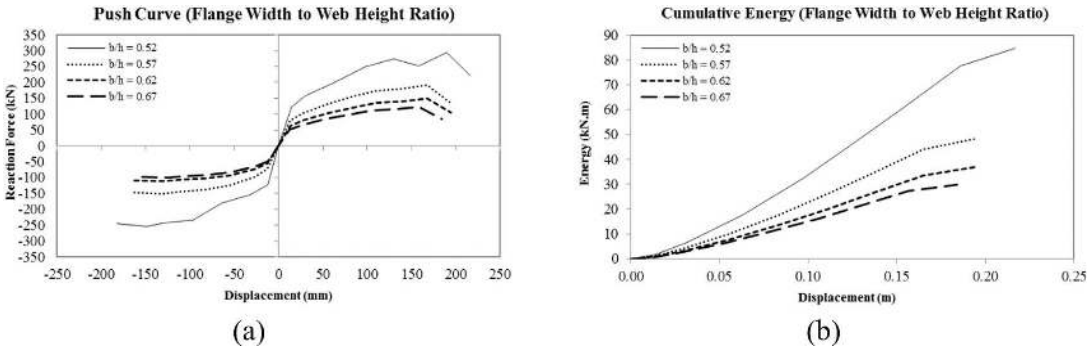

Figure 15. (a) Load – displacement envelop curve and (b) plot of cumulative energy of beam – column connection in the studied samples with different aspect ratios.

3.1.3. Plastic strain

Contours of plastic strain were analyzed to investigate the connection and different members of the studied structural system in terms of mechanical capacity and structural properties of the material. Figure 16 points out the contours of plastic strain in the studied samples with different aspect ratios. Moreover, Figure 17 presents the contours of plastic strain for the seat plates, top separator, and SSD. Looking at Figure 16, it is evident that the level of plastic strain decreases with increasing the aspect ratio. At an aspect ratio of 0.52, the plastic strain affected the web plate, areas in the vicinity of the plastic hinge and the base flange in the middle part of the beam. As the aspect ratio increased to 0.57 and even higher values, however, the plastic strain became limited to areas near the plastic hinge and near the loading position, respectively. Similarly, position of the plastic strain on the connection plates shifted from the vicinity of the plastic hinge to the SSD face. Given the results presented in Figures 16 and 17, it is clear that an increase in the aspect ratio tends to make the connection more brittle and shift the position of plastic strain.

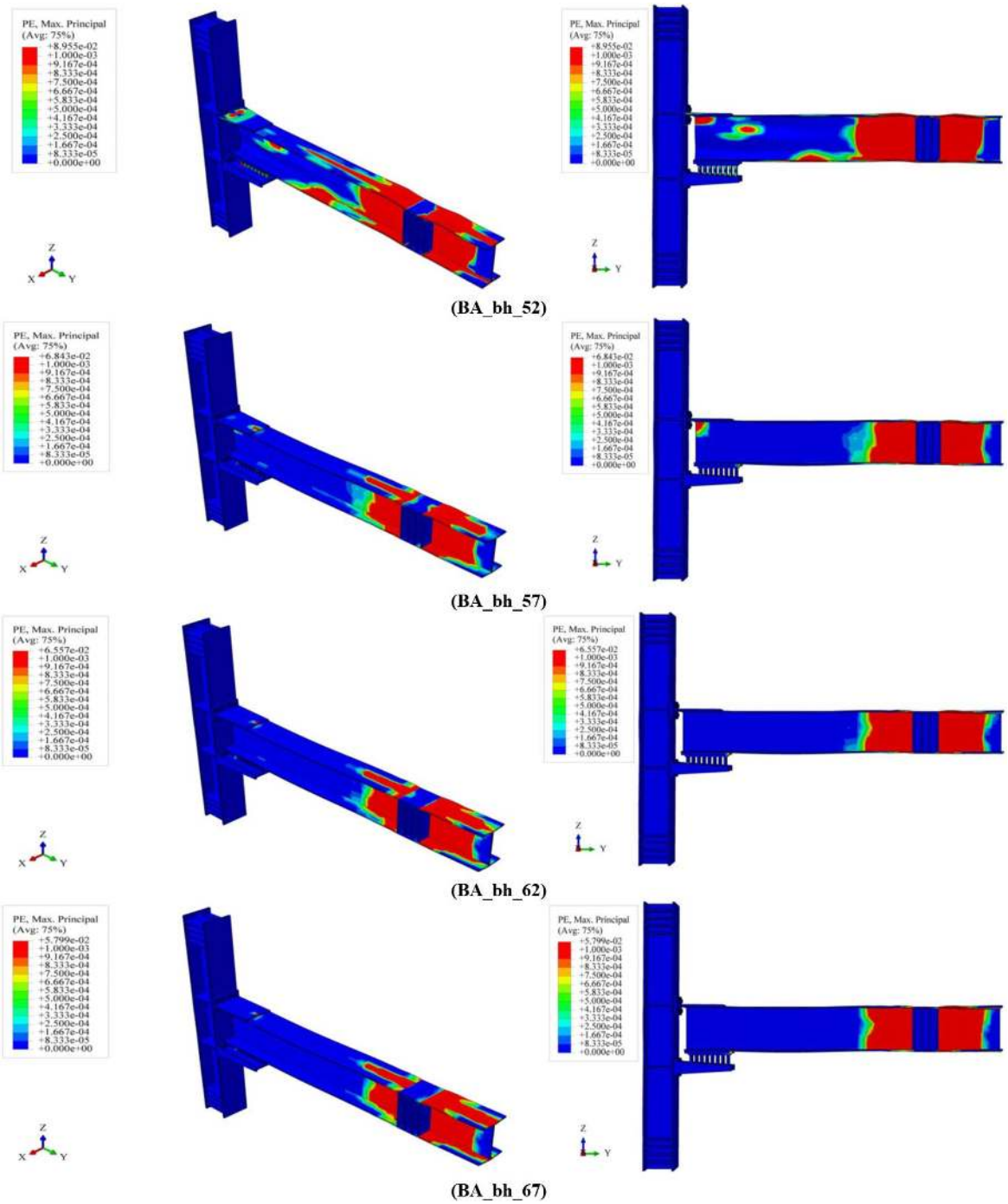

Figure 16. A normal-to-loading-plane perspective view to contours of plastic strain for the studied samples with different aspect ratios.

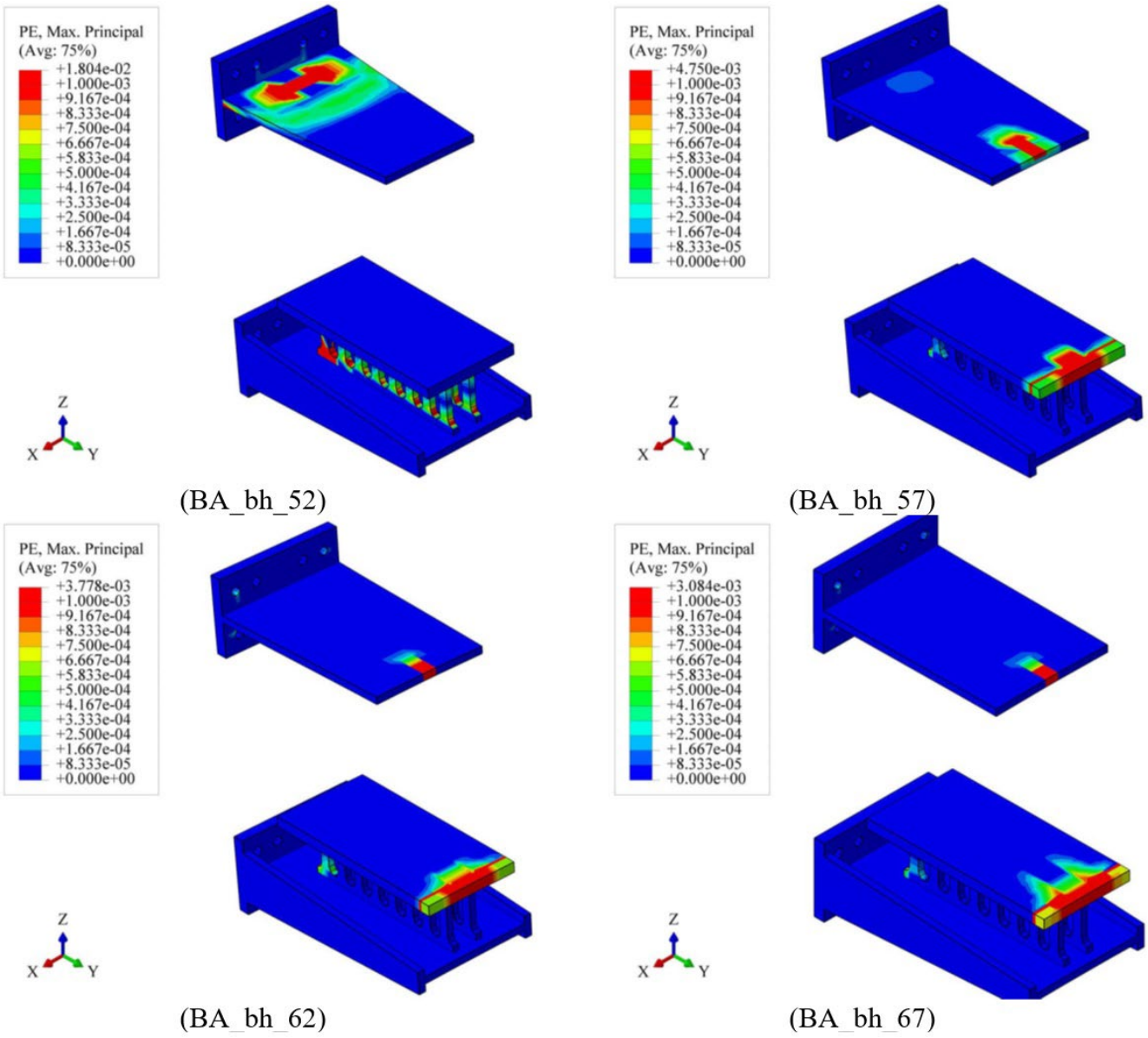

Figure 17. Contours of plastic strain in the split-T seat, top separator plate, and beam-column SSD for the studied samples with different aspect ratios.

3.1.4. Stress contour

Figure 18 shows contours of stress for the studied samples with different aspect ratios. Yielding of the top connection in the sample with an aspect ratio of 0.72 and buckling of the beam web in the same sample coupled with reduced yield volume and absence of buckling prove the hypothesis of reduced formability with increasing the aspect ratio.

3.2. SSD axis to column face distance ratio

The SSD axis to column face distance ratio affects the connection by changing the yield characteristics of the hinge, and absorbable hear moment and force at the beam-column connection. Figure 19 presents a lateral view of the numerical models with different SSD axis to column face distance ratios.

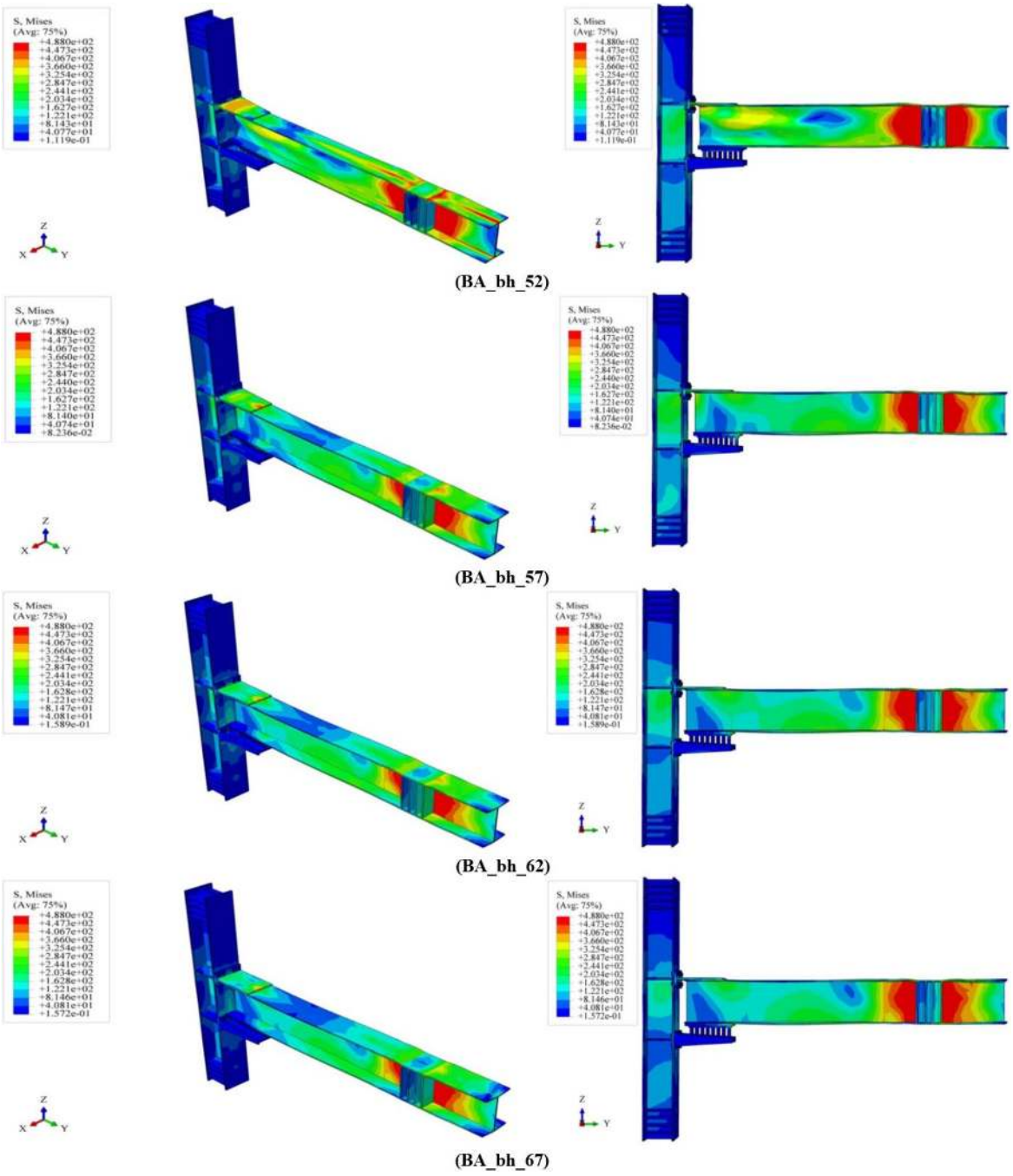

Figure 18. A normal-to-loading-plane perspective view to contours of stress for the studied samples with different aspect ratios.

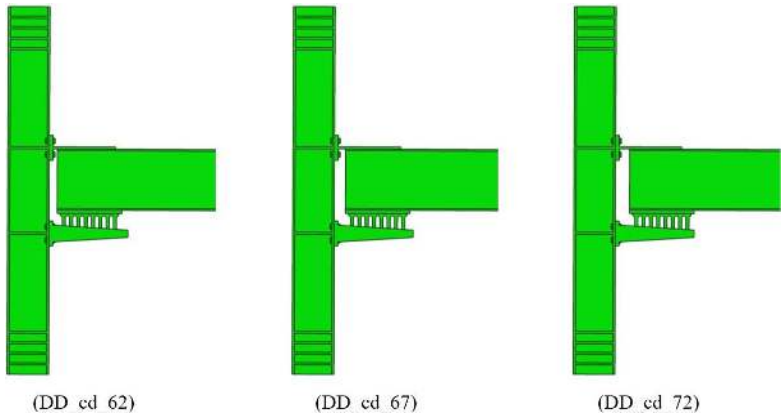

Figure 19. Lateral view of the numerical models with different SSD axis to column face distance ratios.

3.2.1. Connection rotation hysteresis curve

By evaluating the hysteresis curve for different distance ratios, one can select the optimal distance for retaining the required level of formability for the SSD-installed connection. Figure 20 shows rotation-bending moment hysteresis curve considering the rotation hinge at the top corner of the beam-column connection plate in models of different distance ratios. As detailed in Table 6, we herein investigated three distance ratios, namely 0.62, 0.67, and 0.72. the hysteresis curves presented in Figure 20 show that a decrease in the distance ratio imposes no significant impact on the width of the hysteresis curve but insignificantly increases the rotation of the plastic hinges. The difference in ultimate rotation between the smallest and largest distance ratios studied in this work was about 1.16%. therefore, one can conclude that neither a decrease nor an increase in the distance ratio can significantly affect the rotation capacity and load-bearing capacity (and hence energy absorption capacity) of the connection.

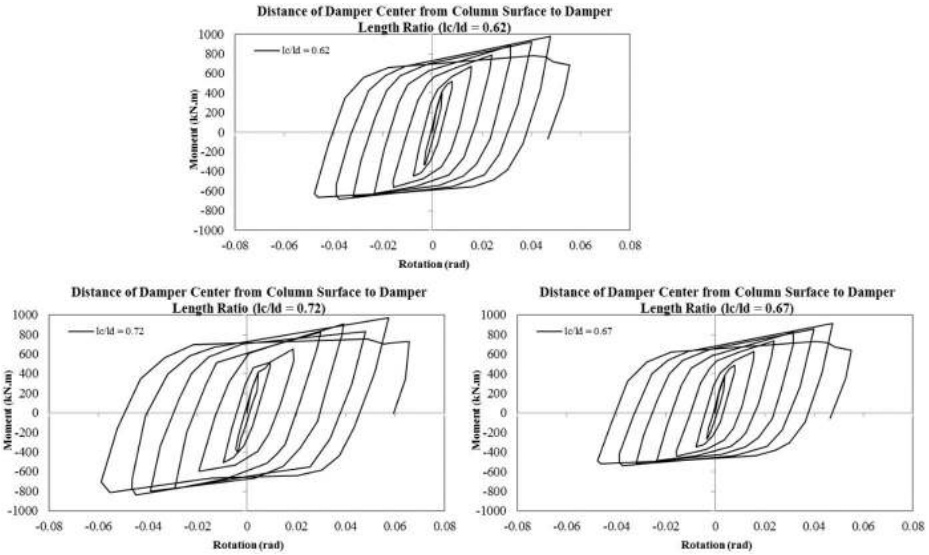

Figure 20. Rotation-bending moment hysteresis curve considering the rotation hinge at the top corner of the beam-column connection plate in models of different SSD axis to column face distance ratios.

3.2.2. Displacement and energy envelop curves

Figure 21 shows the load– displacement envelop curve and cumulative energy for the beam-column connection at different distance ratios. The presented curves can be employed to evaluate the formability and behavior of the connection up to the failure. A comparison between different displacement envelop curves shows that an increase in the distance ratio imposes no significant change in the energy absorption and load-bearing capacity of the connection. The remarkable increase in the deformation at failure of the sample with a distance ratio of 0.72 indicates its superiority over other samples with different distance ratios. In particular, ultimate strength increased by 8% as the distance ratio increased from 0.62 to 0.67. This has been while the sample with a distance ratio of 0.72 exhibited 4% lower ultimate strength than the one with a distance ratio of 0.67. Ultimate energy absorption capacity of the sample with a distance ratio of 0.72 was 45% and 26% higher than those with distance ratios of 0.76 and 0.62, respectively, proving its superior performance.

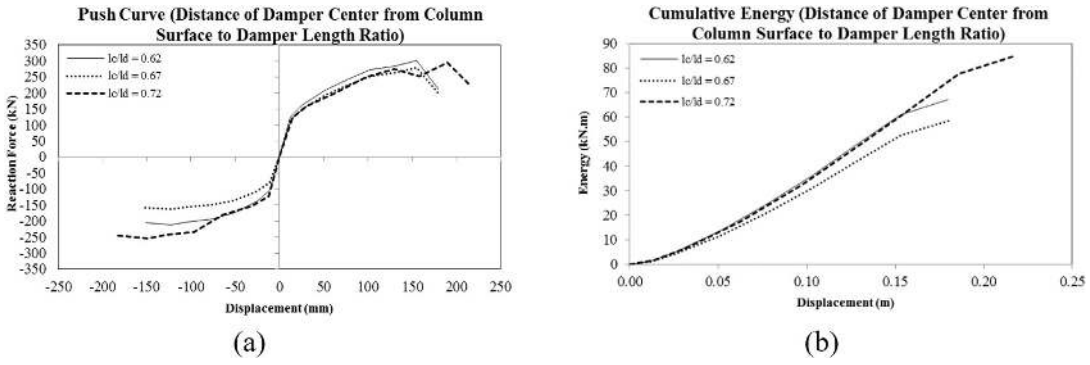

Figure 21. (a) Load – displacement envelop curve and (b) plot of cumulative energy of beam – column connection in the studied samples with different SSD axis to column face distance ratios.

3.2.3. Plastic strain

Figure 22 points out the contours of plastic strain in the studied samples with different distance ratios. The figure shows evidently that the level of plastic strain of the connection does not change significantly. For all samples, the plastic strain occurred in the vicinity of the plastic hinge and the base flange in the middle part of the beam. As the distance ratio increased, the level of plastic strain in the base flange near the mentioned zone increased significantly. As a general conclusion, the connection performance exhibited no significant change with varying the distance ratio.

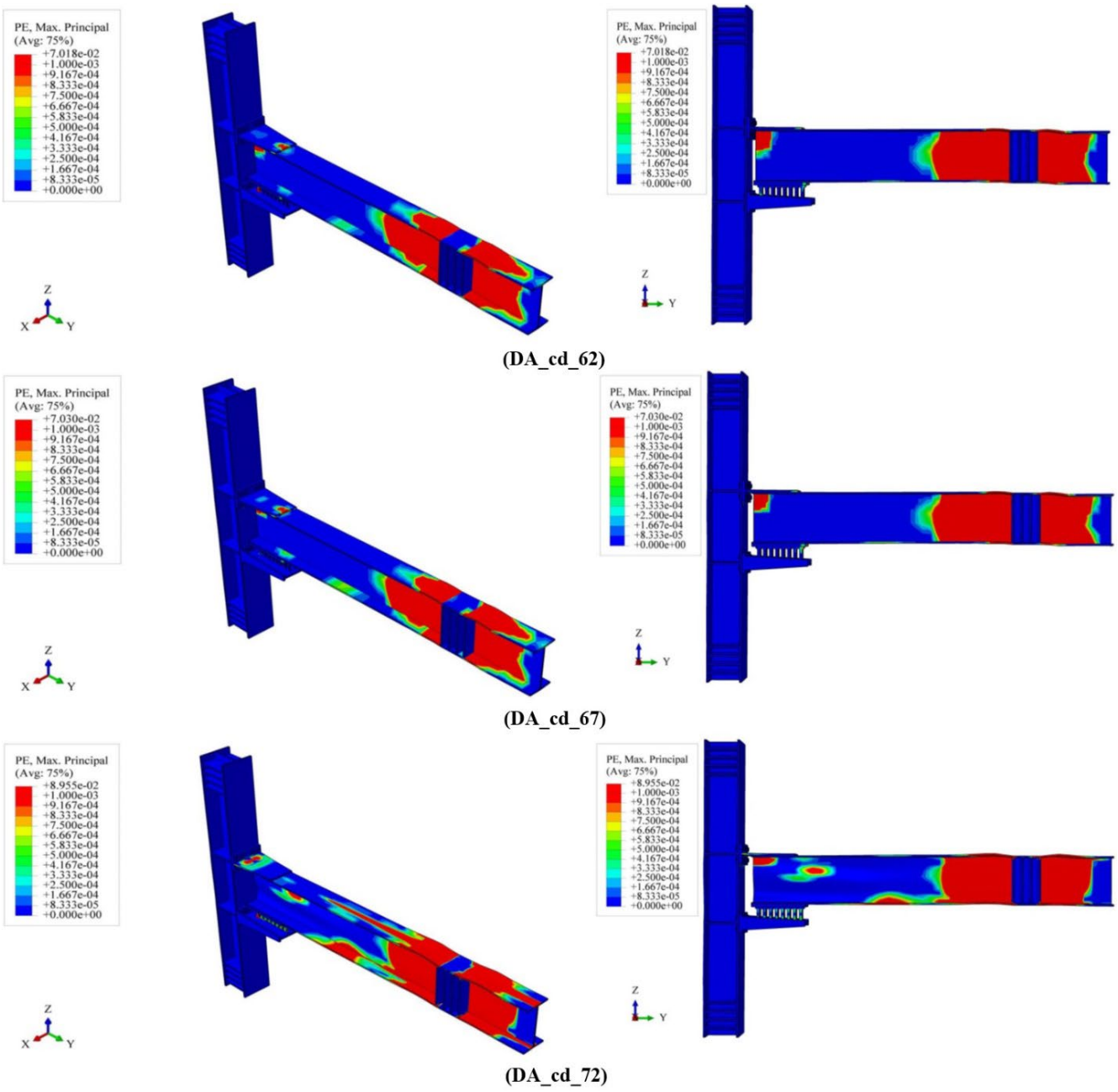

Figure 22. A normal-to-loading-plane perspective view to contours of plastic strain for the studied samples with different SSD axis to column face distance ratios.

3.2.4. Stress contour

Figure 23 shows contours of stress for the studied samples with variable distance ratios. Yielding of the top connection in all samples and development of a similar stress pattern in different components indicates insignificant effect of the distance ratio and hence confirming the findings of other subsections discussing the distance ratio.

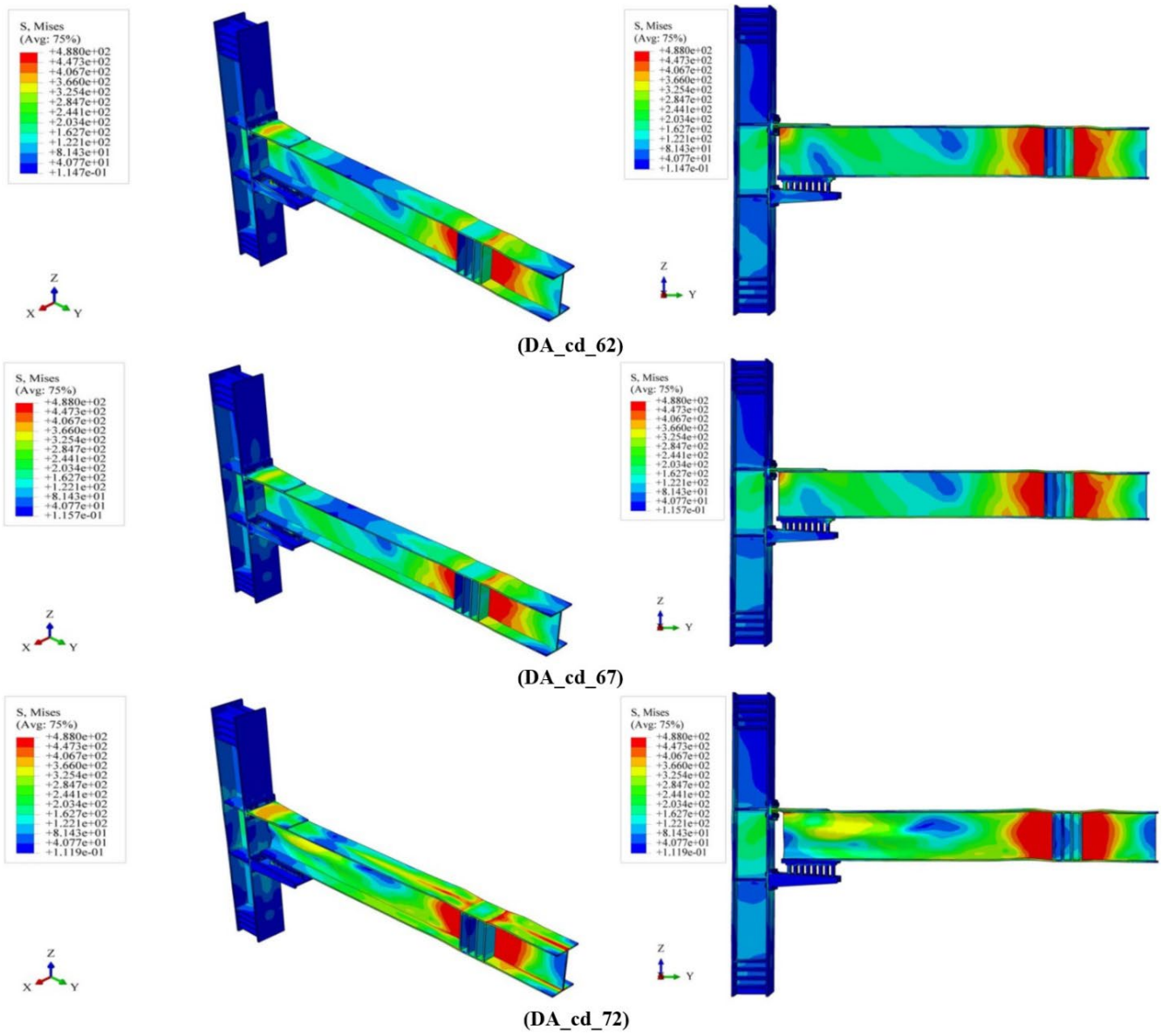

Figure 23. A normal-to-loading-plane perspective view to contours of stress for the studied samples with different SSD axis to column face distance ratios.

3.3. Damper compactness ratio

Damper compactness ratio refers to the ratio of damper support width (considering all supports) to total width of the damper (including the slits). A change in the compactness ratio can affect the overall behavior of the connection by altering the damper mechanism. Therefore, this ratio was evaluated as a primary factor in the present study. In respect, we considered three compactness ratios, namely 0.34, 0.43, and 0.51.

3.3.1. Connection rotation hysteresis curve

By evaluating the hysteresis curve for different compactness ratios, one can understand the mechanism of the SSD assuming constant material behavior. Figure 24 shows rotation-bending moment hysteresis curve considering the rotation hinge at the top corner of the beam-column connection plate in models of different compactness ratios. The hysteresis curves presented in Figure 24 indicate that a decrease in the compactness ratio narrows down the width of the hysteresis curve significantly. Such a reduction in the compactness ratio further lowers the rotation around the plastic hinge of the top plate of the beam-column connection. The difference in ultimate rotation between the smallest and largest compactness ratios studied in this work was about 71%. In conclusion, a reduction in the compactness ratio can significantly reduce the rotation capacity and load-bearing capacity (and hence energy absorption capacity) of the connection, as per the hysteresis curves.

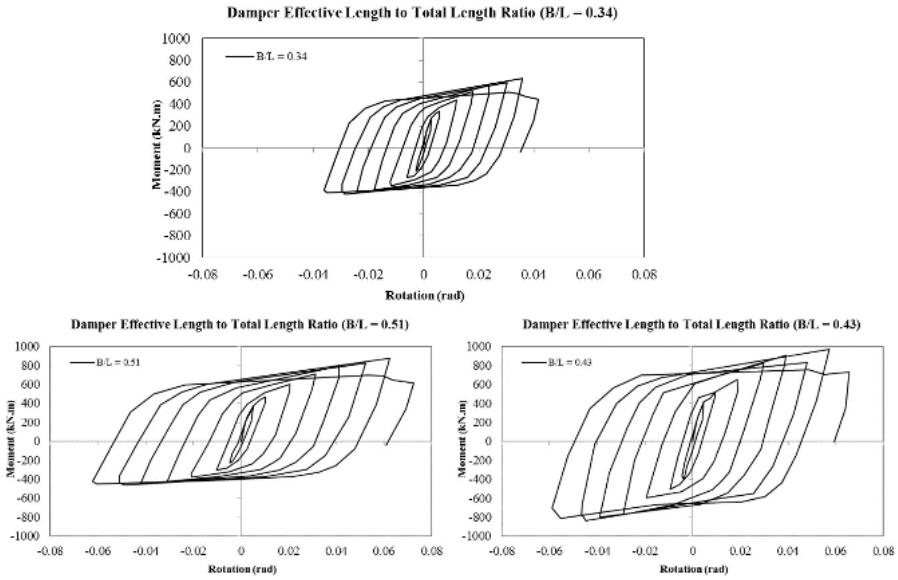

Figure 24. Rotation-bending moment hysteresis curve considering the rotation hinge at the top corner of the beam-column connection plate in models of different damper compactness ratios.

3.3.2. Displacement and energy envelop curves

Figure 25 shows the load– displacement envelop curve and cumulative energy for the beam-column connection at different compactness ratios. An increase in the compactness increases the energy absorption and load-bearing capacity of the connection. The sample with a compactness ratio of 0.34 exhibited some 50% difference with those with compactness ratios of 0.43 and 0.51, indicating its improper performance. The subtle difference in deformation between the compactness ratios of 0.43 and 0.51 suggests that excessive increase in the compactness ratio would no longer affect the ultimate displacement of the connection and rather limits the energy absorption by reducing the ultimate load-bearing capacity of the connection. In particular, ultimate strength increased by 64% and 18% as the compactness ratio changed from 0.43 to 0.34 and 0.51, respectively. Ultimate energy absorption capacity of the sample with a compactness ratio of 0.43 was 164% and 19% higher than those with compactness ratios of 0.34 and 0.51, respectively.

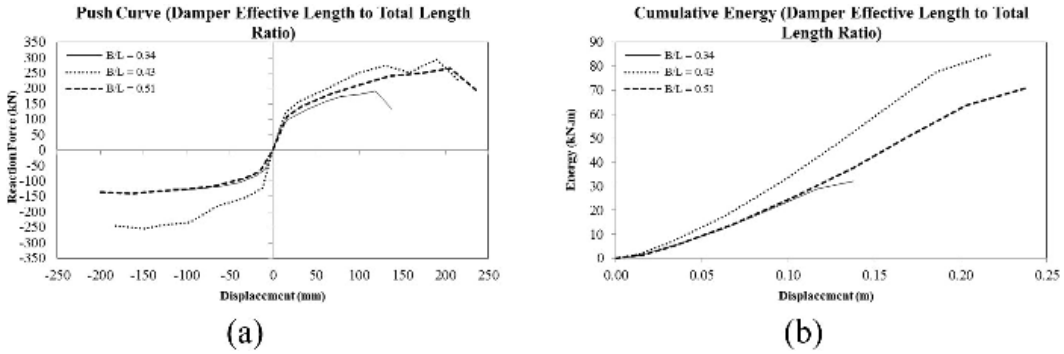

Figure 25. (a) Load – displacement envelop curve and (b) plot of cumulative energy of beam – column connection in the studied samples with different damper compactness ratios.

3.3.3. Plastic strain

Figure 26 points out the contours of plastic strain in the studied samples with different compactness ratios. A decrease in the compactness ratio tends to shift the plastic strain-affected area toward the point where the cyclic load is applied, thereby boosting the deformation in the vicinity of the load exertion point. Development of the plastic strain was observed in the vicinity of the plastic hinge for all models and at the base flange of the beam for the models corresponding to the compactness ratios of 0.43 and 0.51. As the compactness ratio increased, the level of plastic strain in the base flange near the mentioned zone increased significantly. As a general conclusion, the connection performance exhibited no significant change with varying the compactness ratio. Figure 27 depicts the plastic strain contour for the SSD in the studied samples with different compactness ratios. According to this figure, it is evident that some plastic strain has occurred at the bottom end of the model near the column for all SSDs. The plastic strain is also evident at the top end of the model with compactness ratio of 0.51 in the vicinity of the beam.

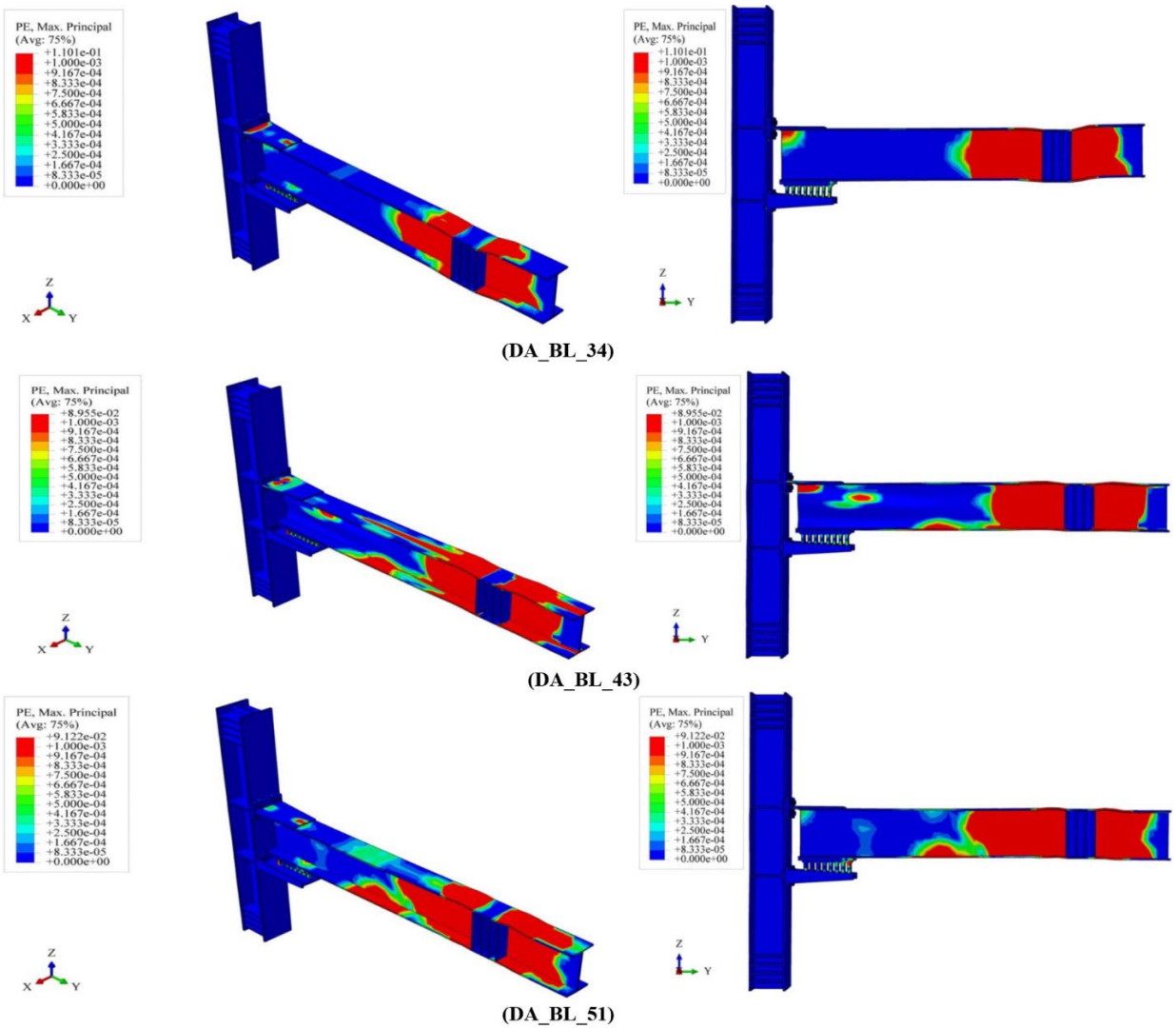

Figure 26. A normal-to-loading-plane perspective view to contours of plastic strain for the studied samples with different compactness ratios.

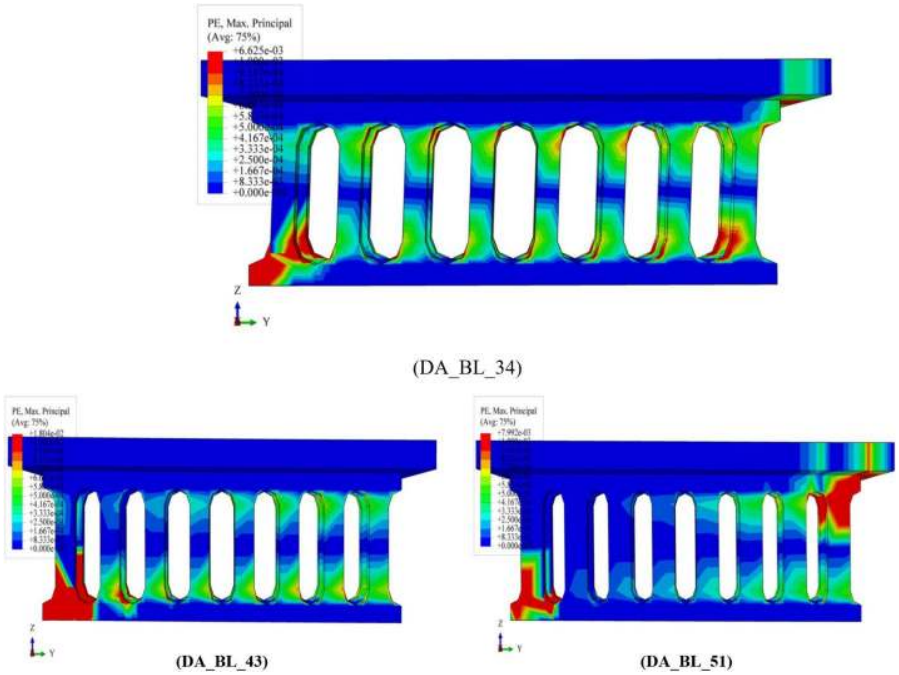

Figure 27. Contours of plastic strain of the SSD for the studied samples with different compactness ratios.

3.3.4. Stress contour

Figure 28 shows contours of stress for the studied samples with variable compactness ratios. The buckling of the beam web and flange at the end of the model with a compactness ratio of 0.34 and also buckling of the beam web in the vicinity of the beam-column connection in the model with a compactness ratio of 0.43 were observed. Moreover, the samples with compactness ratios of 0.43 and 0.51 exhibited yielding at the top connection.

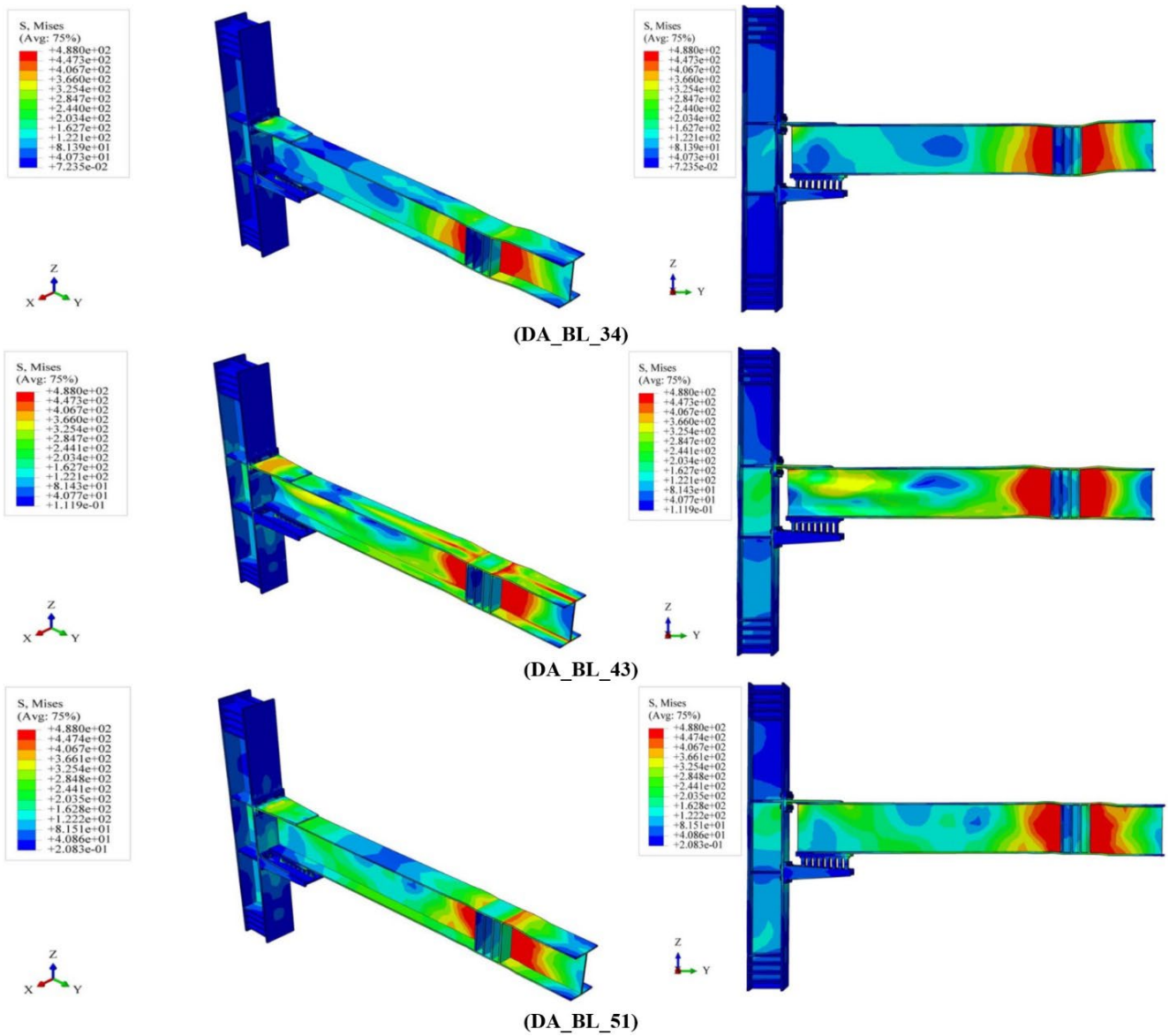

Figure 28. A normal-to-loading-plane perspective view to contours of stress for the studied samples with different damper compactness ratios.

3.4. Damper to beam flange thickness ratio

The damper to beam flange thickness ratio is important because of its impact on the connection stiffness. A change in the connection stiffness contributes to the connection formability and hence behavioral performance of the structural system. This was why we considered the damper to beam flange thickness ratio as an important factor in this study. As detailed in Table 6, we herein considered three thickness ratios, namely 1.00, 1.12, and 1.24.

3.4.1. Connection rotation hysteresis curve

By evaluating the hysteresis curve for different thickness ratios, one can understand the changes in the damper stiffness ratio. Figure 29 shows rotation-bending moment hysteresis curve considering the rotation hinge at the top corner of the beam-column connection plate in models of different thickness ratios. A decrease in the thickness ratio

incoherently increases/decreases the width of the hysteresis curve. Indeed, the maximum width of the hysteresis curve was observed at a thickness ratio of 1.12. With increasing the thickness ratio, the rotation around the plastic hinge of the top plate of the beam-column connection increases. The difference in ultimate rotation between the smallest and largest thickness ratios studied in this work was 19%.

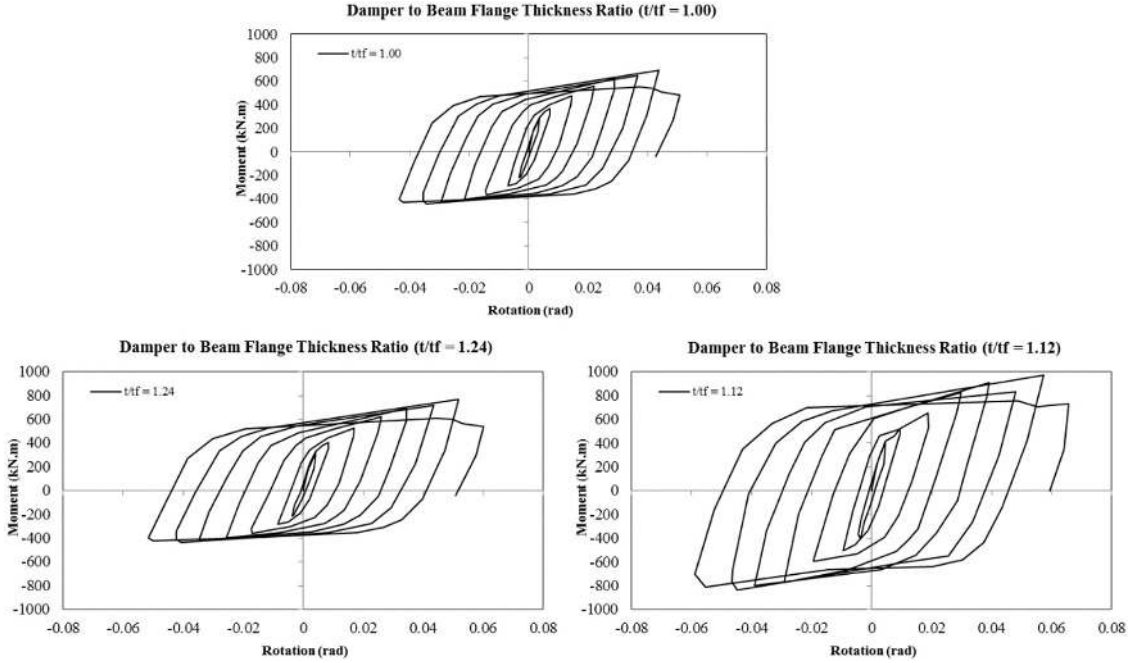

Figure 29. Rotation-bending moment hysteresis curve considering the rotation hinge at the top corner of the beam-column connection plate in models of different damper to beam flange thickness ratios.

3.4.2. Displacement and energy envelop curves

Figure 30 presents the load– displacement envelop curve and cumulative energy for the beam-column connection at different thickness ratios. Maximum energy absorption and load-bearing capacity were observed at a thickness ratio of 1.12. The displacement and cumulative energy envelop curves of the beam connection indicated that the thickness ratios 1.00 and 1.24 were marginally better than the thickness ratio of 1.24, with the former two being more or less similar to one another. In turn, the energy absorption and load-bearing capacity of the model with a thickness ratio of 1.12 were 61% and 36% higher than those of the model with a thickness ratio of 1.24, and also 103% and 51% higher than the model with a thickness ratio of 1.00, indicating the superior performance of the model with a thickness ratio of 1.12, as compared to other thickness ratios investigated in the present research.

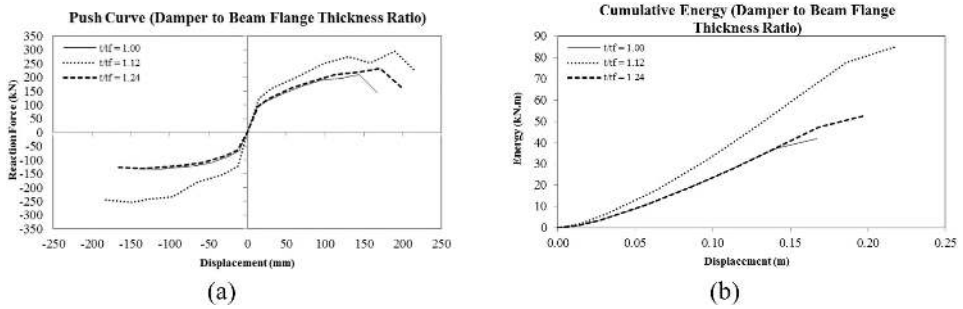

Figure 30. (a) Load – displacement envelop curve and (b) plot of cumulative energy of beam – column connection in the studied samples with different damper to beam flange thickness ratios.

3.4.3. Plastic strain

Figure 31 points out the contours of plastic strain in the studied samples with different thickness ratios. The models with thickness ratios of 1.00 and 1.24 exhibited significant degrees of similarity. All models showed plastic strain in the vicinity of the plastic hinge. Figure 32 shows the plastic strain from the column face to the beam, connection plate, and SSD. The models with thickness ratios of 1.00 and 1.24 were highly similar in terms of plastic strain development.

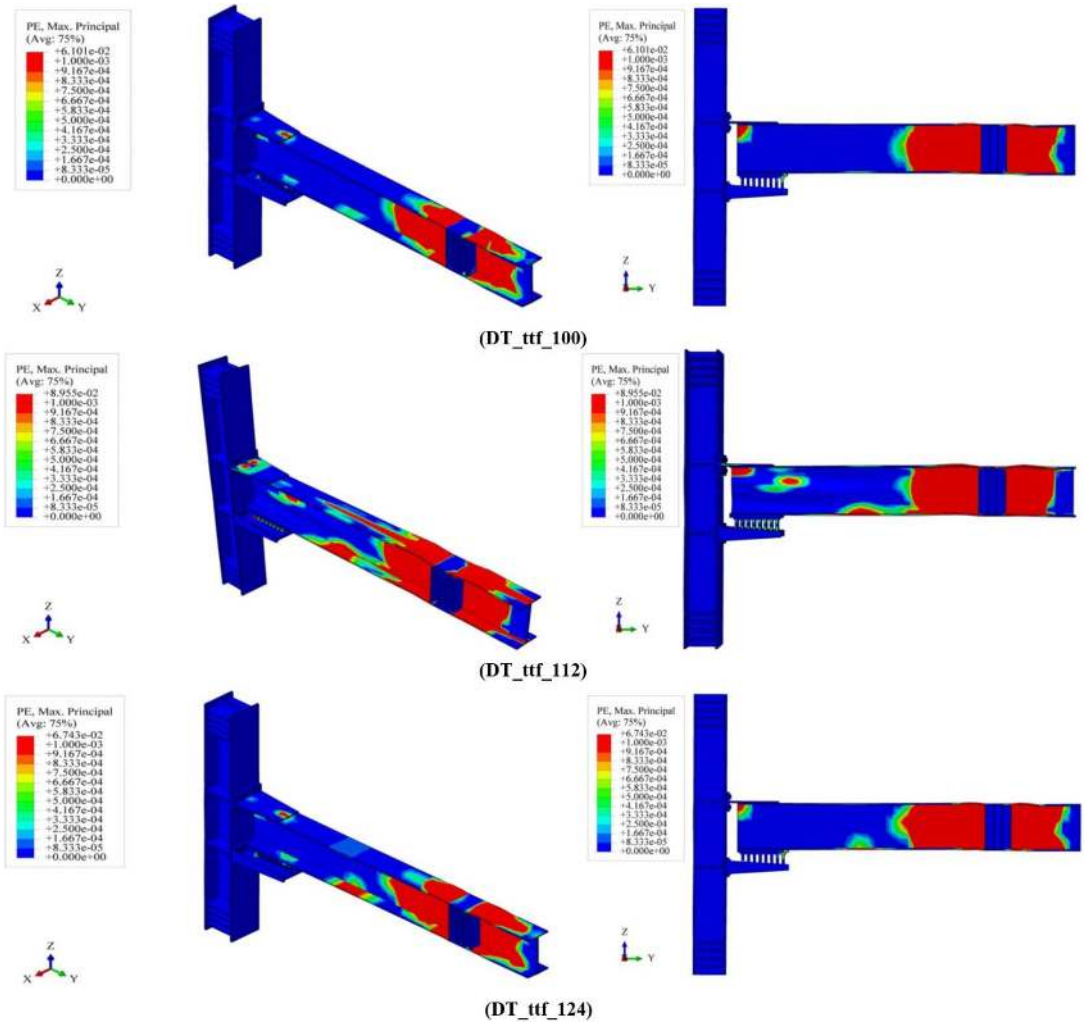

Figure 31. A normal-to-loading-plane perspective view to contours of plastic strain for the studied samples with different damper to beam flange thickness ratios.

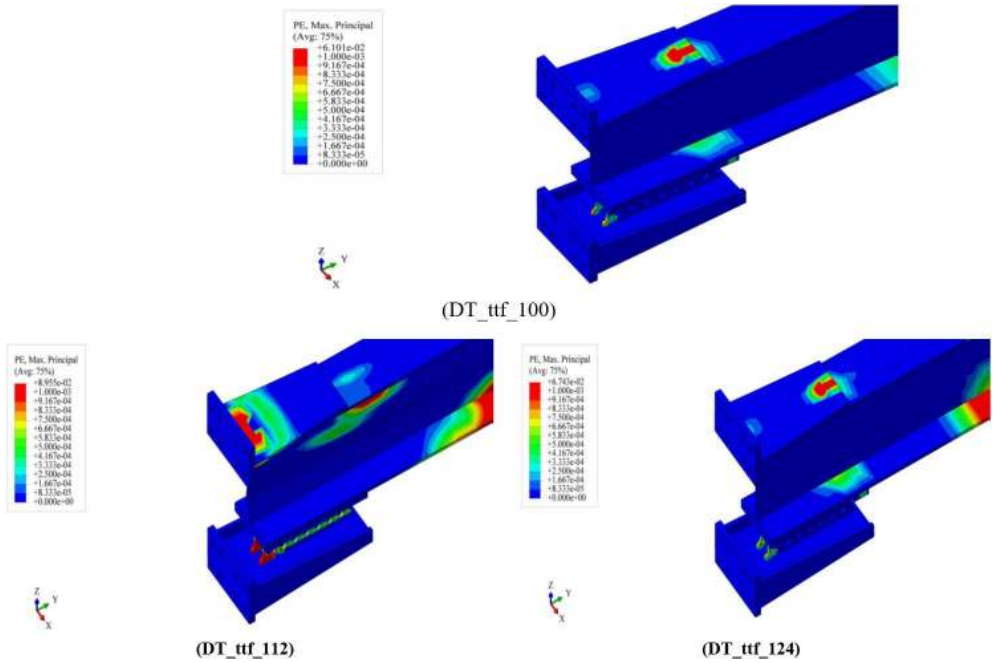

Figure 32. Contours of plastic strain of the beam, connection plates, and SSD from the column face for the studied samples with different damper to beam flange thickness ratios.

3.4.4. Stress contour

Figure 33 shows contours of stress for the studied samples with variable thickness ratios. Similar stress contours, alongside other parameters, were obtained for the models with thickness ratios of 1.00 and 1.24, indicating similarity in connection performance between these two models. Given the superiority of the results for the thickness ratio of 1.12, it was most probably the optimal thickness ratio.

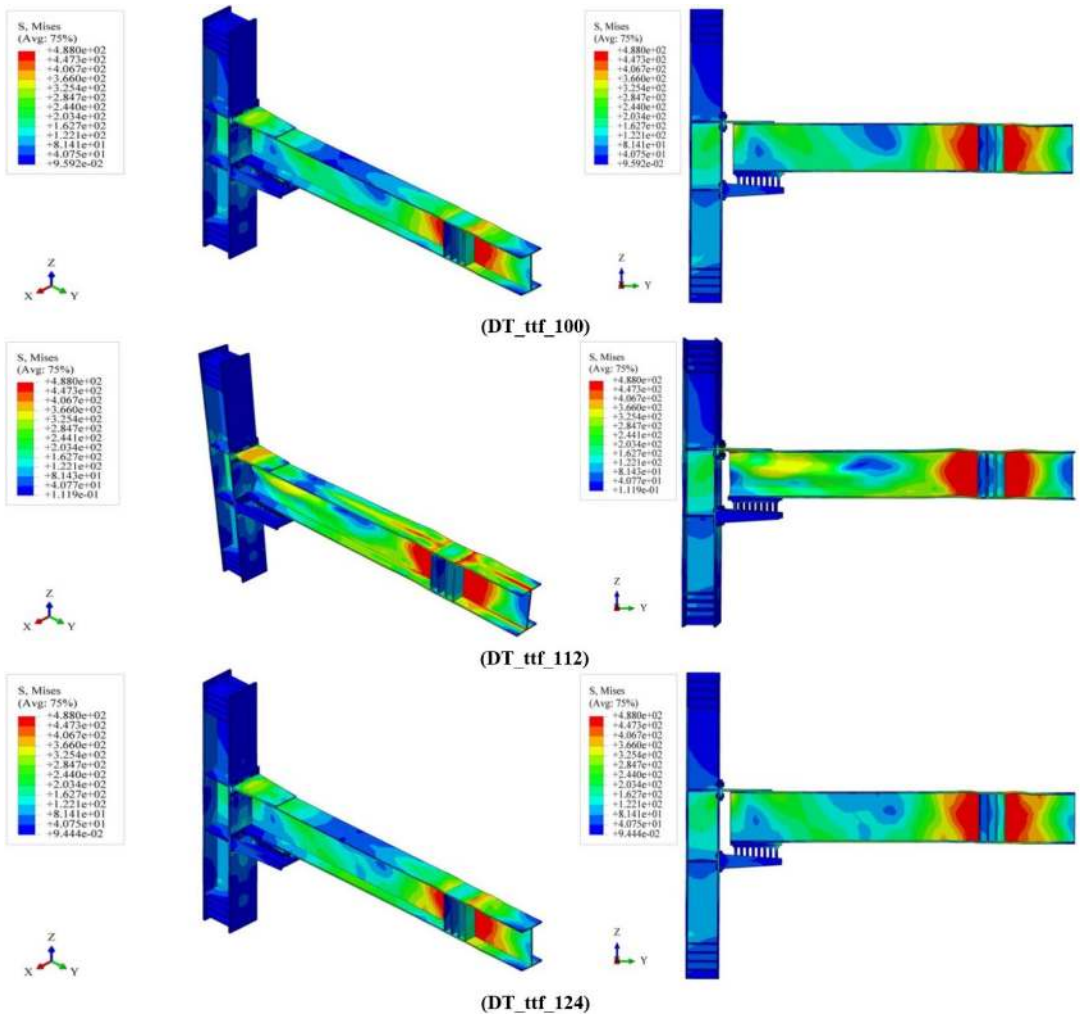

Figure 33. A normal-to-loading-plane perspective view to contours of stress for the studied samples with different damper to beam flange thickness ratios.

3.5. Comparison of the results

In this research, four parameters were considered to evaluate the behavior of connections across a moment frame system equipped with SSD. These included aspect ratio, distance ratio, compactness ratio, and thickness ratio. Based on the results, it was generally found that an increase in the aspect ratio reduces the connection performance while an increase in the thickness and compactness ratios adds to the rotation capacity of the connection. On the other hand, variations of the distance ratio were found not to significantly affect the performance, load-bearing, and rotation capacities of the connection. Figure 34 presents the variation of beam rotation with changes in different parameters evaluated in this work. Figure 35 demonstrates the plot of dissipated energy at the beam-column connection for different values of different ratios. According to Figures 34 and 35, it is evident that an increase in the aspect ratio lowers the rotation capacity of the connection. The sharp increase in the rotation capacity, as seen on the plot of compactness ratio, indicates the high sensitivity of the connection to changes in this ratio. Moreover, by evaluating the curves of dissipated energy in Figure 35, it is clear that the samples with a compactness ratio of 0.34, thickness ratio of 1.00, distance ratio of 0.67, and aspect ratios of 0.62 and 0.67 tend to exhibit the most undesired performances. Therefore, it can be concluded that an increase in the aspect ratio, a decrease in the distance ratio, and a change in the thickness ratio tend to lower the performance of an SSD.

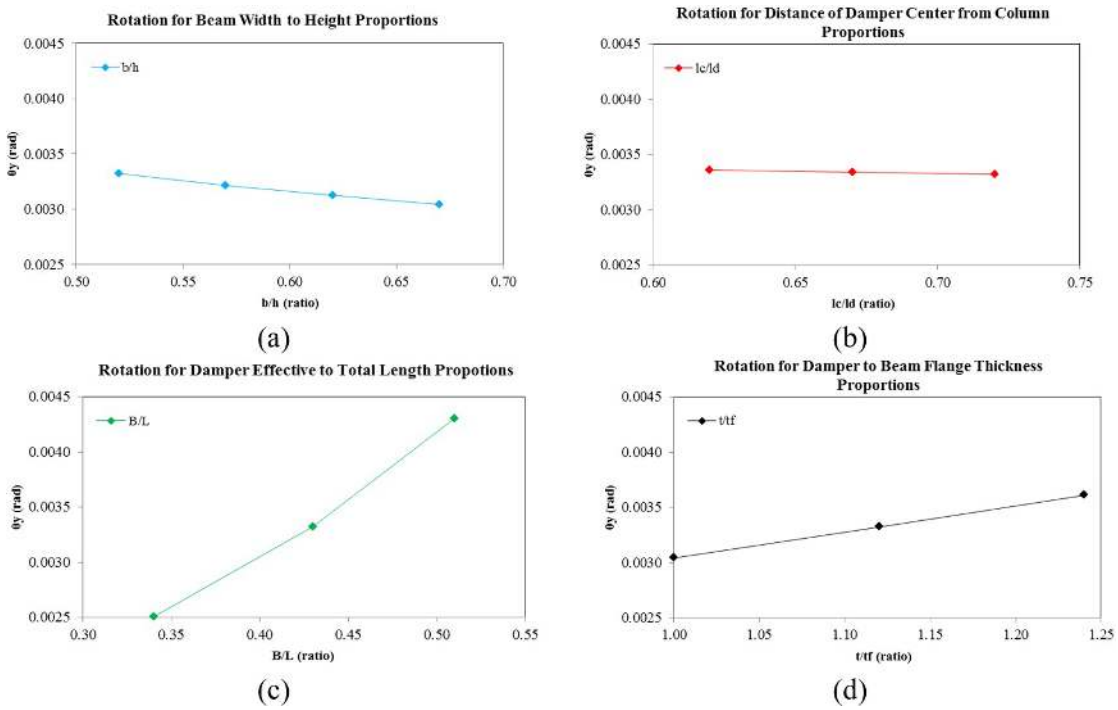

Figure 34. Variations of beam rotation against changes in the parameters studied in this work: (a) aspect ratio, (b) distance ratio, (c) compactness ratio, and (d) thickness ratio.

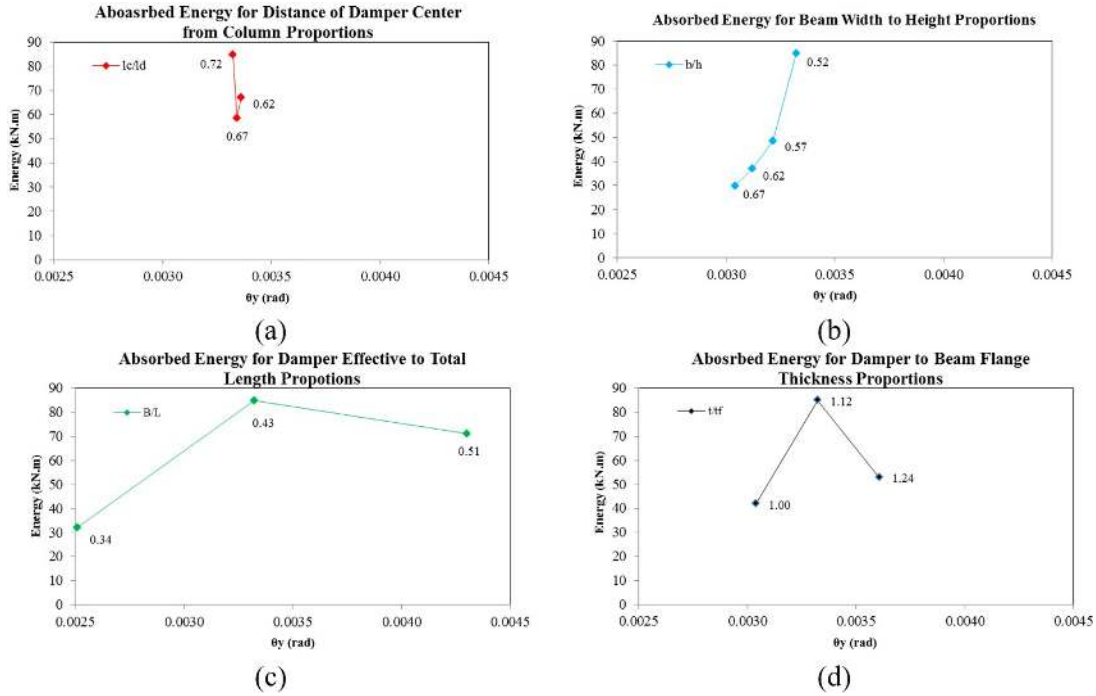

Figure 35. Variations of dissipated energy against changes in the parameters studied in this work: (a) aspect ratio, (b) distance ratio, (c) compactness ratio, and (d) thickness ratio.

Table 10 reports contours of maximum plastic strain and stress for different models. Based on the results of this table, it is evident that the maximum plastic strain was associated with the sample at a compactness ratio of 0.43 followed by the one at 0.51. Evaluating the mentioned ratios, it is observed that the hysteresis curve drops significantly despite the increase in formability. This suggests that the numerical model with an aspect ratio of 0.52 is still the best-performing model among all of the studied numerical models. Given that all components of the model yielded, maximum stress occurred near ultimate stress of the beam for all models, which led to failure and termination of numerical analysis.

Table 10. maximum values of plastic strain and stress in different numerical models.

Model Name	Max stress	Max strain
	N/mm^2	mm/mm
BA_bh_52	488	0.089
BA_bh_57	488	0.068
BA_bh_62	488	0.066
BA_bh_67	487	0.058
DD_cd_62	488	0.070
DD_cd_67	488	0.070
DD_cd_72	488	0.089
DA_BL_34	488	0.110
DA_BL_43	488	0.089
DA_BL_51	488	0.091
DT_ttf_100	488	0.061
DT_ttf_112	488	0.089
DT_ttf_124	488	0.067

4. Conclusion

In this research, the behavior of connections in a moment frame system equipped SSD was investigated parametrically. For this purpose, effects of changes in four parameters on the connection behavior were studied; these included aspect ratio, distance ratio, compactness ratio, and damper thickness ratio. Based on the results, the following conclusions could be drawn.

1. It was generally found that an increase in the aspect ratio reduces the connection performance while an increase in the thickness and compactness ratios adds to the rotation capacity of the connection. Variations of the distance ratio were found not to affect any significant impact on the performance and load-bearing and rotation capacities of the connection.
2. With increasing the aspect ratio, the hysteresis curve is narrowed down significantly. It further leads to an insignificant reduction in the plastic hinge rotation capacity. The difference in ultimate rotation between the largest and smallest aspect ratios was about 9.23%. Accordingly, an increase in the aspect ratio tends to slenderize the hysteresis curves while insignificantly limiting the rotation capacity and lowering the load-bearing capacity of the connection (and hence its energy absorption capacity). A decrease in the distance ratio was seen not to impose any significant effect on the width of the hysteresis curve. Similarly, such a change led to a barely insignificant increase in the plastic hinge rotation capacity. The difference in ultimate rotation between the largest and smallest distance ratios was as low as 1.16%, proving that changes in the distance ratio impose no significant effects on the rotation or load-bearing capacities of the connection and hence its energy absorption capacity, as per the hysteresis curves.
3. A reduction in the compactness ratio tends to significantly lower the width of the hysteresis curve. This reduction further lowers the plastic hinge radiation in the top plate of the beam-column connection abruptly. In general, a reduction in the compactness ratio significantly reduces the rotation and load-bearing capacities as well as the hysteresis curve energy absorption. The difference in ultimate rotation between the largest and smallest compactness ratios was 71%. A change of thickness ratio led to heterogenous changes in the width of the hysteresis curve. In other words, the maximum width of hysteresis curve corresponded to a thickness ratio of 1.12. With increasing the thickness ratio, the plastic hinge radiation in the top plate of the beam-column connection increases. The difference in ultimate rotation between the largest and smallest thickness ratios was 19%.
4. Comparing the displacement envelop curves showed that an increase in the aspect ratio decreases the energy absorption and load-bearing capacities of the connection. The model with an aspect ratio of 0.52 shows 39% and 61% higher ultimate strength than those with aspect ratios of 0.57 and 0.72, respectively. With increasing the distance ratio, no significant change was observed in the energy absorption and load-bearing capacities of the connection. The significant increase in the deformation at failure of the connection in the sample with a distance ratio of 0.72 was an indication of the superior performance of this sample compared to other distance ratios. The sample with a distance ratio of 0.62 exhibited 8% higher and 4% lower ultimate strengths than the samples with distance ratios of 0.67 and 0.72, respectively. The sample with a

distance ratio of 0.72 exhibited 45% and 26% higher energy absorption capacities than those with distance ratios of 0.67 and 0.62, respectively, indicating its superior performance.

5. The energy absorption and load-bearing capacities increase with the compactness ratio. The sample with a compactness ratio of 0.34 ended up with a deformation equal to about 50% of those with the samples at compactness ratios of 0.43 and 0.51, indicating its inappropriate performance. The displacement and cumulative energy envelop curves of the beam-column connection indicated that the thickness ratios of 1.00 and 1.24 were marginally better than the thickness ratio of 1.24, with the former two being more or less similar to one another. The energy absorption and load-bearing capacity of the model with a thickness ratio of 1.12 were 61% and 36% higher than those of the model with a thickness ratio of 1.24, and also 103% and 51% higher than the model with a thickness ratio of 1.00, indicating the superior performance of the model with a thickness ratio of 1.12, as compared to other thickness ratios.
6. The level of plastic strain decreases with increasing the aspect ratio. At an aspect ratio of 0.52, the plastic strain affected the web plate, areas in the vicinity of the plastic hinge and the base flange in the middle part of the beam. As the aspect ratio increased to 0.57 and even higher values, however, the plastic strain became limited to areas near the plastic hinge and near the loading position, respectively. Similarly, position of the plastic strain on the connection plates shifted from the vicinity of the plastic hinge to the SSD face. Accordingly, increased brittleness of the connection with increasing the aspect ratio and the shift of the position of plastic strain were observed. Yielding of the top connection in the sample with an aspect ratio of 0.72 and buckling of the beam web in the same sample coupled with reduced yield volume and absence of buckling prove the hypothesis of reduced formability with increasing the aspect ratio.
7. The plastic strain exhibited no significant change for various distance ratios. For all samples, the plastic strain occurred in the vicinity of the plastic hinge and the base flange in the middle part of the beam. As the distance ratio increased, the level of plastic strain in the base flange near the mentioned zone increased significantly. As a general conclusion, the connection performance exhibited no significant change with varying the distance ratio. Yielding of the top connection in all samples and development of a similar stress pattern in different components indicates insignificant effect of the distance ratio and hence confirming the relevant findings.
8. A decrease in the compactness ratio tends to shift the plastic strain-affected area toward the point where the cyclic load is applied. Development of the plastic strain was observed in the vicinity of the plastic hinge for all models and at the base flange of the beam for the models corresponding to the compactness ratios of 0.43 and 0.51. Some plastic strain has occurred at the bottom end of the model near the column for all SSDs. The plastic strain is also evident at the top end of the model with compactness ratio of 0.51 in the vicinity of the beam. The buckling of the beam web and flange at the end of the model with a compactness ratio of 0.34 and also buckling of the beam web in the vicinity of the beam-column connection in the model with a compactness ratio of 0.43 were observed. Moreover, the samples with compactness ratios of 0.43 and 0.51 exhibited yielding at the top connection.
9. The models with thickness ratios of 1.00 and 1.24 exhibited high degrees of similarity in plastic strain behavior. All models showed plastic strain in the vicinity of the plastic hinge. The models with thickness ratios of 1.00 and 1.24 were highly similar in terms of plastic strain development. Similarity of stress contours among the models of the same thickness ratio indicated their identical connection performance. Given the superiority of the results for the thickness ratio of 1.12, it was most probably the optimal thickness ratio.
10. An increase in the aspect ratio decreases the rotation capacity of the connection. The sharp increase in the rotation capacity indicates the high sensitivity of the connection to changes in this ratio. samples with a compactness ratio of 0.34, thickness ratio of 1.00, distance ratio of 0.67, and aspect ratios of 0.62 and 0.67 tend to exhibit the most undesired performances. Therefore, it can be concluded that an increase in the aspect ratio, a decrease in the distance ratio, and a change in the thickness ratio tend to lower the performance of a SSDs.

Acknowledgment

The writers gratefully acknowledge Ben Chen, Zhen Wang, Han Zhang, Ke Zhou, Xiaoyan Zheng, Shaoyun Zhu, Liqing Liu, Dunben Sun, Jing Cao, Yanjun Liu, Junhong Xu and others from the Nanjing Forestry University for helping.

The research work presented in this paper is supported by the National Natural Science Foundation of China (Nos. 51878354 & 51308301), the Natural Science Foundation of Jiangsu Province (Nos. BK20181402 & BK20130978), Six talent peak high-level projects of Jiangsu Province (No. JZ029), Foreign Young Talents Project China (No. QN2021014006L) and Qinglan Project of Jiangsu Higher Education Institutions.

Authors contribution: Investigation, H Li and H Mahdi ; Conceptualization, H Li; Funding acquisition, H Li; Formal analysis, H Li and H Mahdi ; Writing - original draft, H Li and H Mahdi; Supervision, H Li, C Ileana and C Ottavia; review & editing, C Ileana and C Ottavia

Editor: Marcílio Alves

References

Miller, D.K., (1998). Lessons learned from the Northridge earthquake. Eng Struct, 20(4-6): 249-260.

Park, H.Y., and Oh, S.H., (2020). Structural performance of beam system with T-stub type slit damper, Engineering Structures, 205, ISSN 0141-0296.

Sofias, C.E., Kalfas, C.N., and Pachoumis, D.T., (2015). Experimental and FEM analysis of reduced beam section moment endplate connections under cyclic loading. Engineering Structures, 59, 320-329.

Oh, S.H., Kim, Y.J., (2005). Hysteretic behavior of beam-to-column connections with slit plate dampers. J Archit Inst Korea Struct Constr. 21(12): 101-108.

Kobori, T., Mirura, Y., Fukusawa, E., Yamada, T., Arita, T., Takenaka, Y., et al. (1992). Development and application of hysteresis steel dampers. In: Proceedings of 11th world conference on earthquake engineering. pp. 2341-2346.

Tsai, K., Chen, H., Hong, C., (1993). Design of steel triangular plate energy absorbers for seismic-resistant construction. Earthq Spectra, 9(3): 505-528.

Koken, A., and Koroglu, M.A., (2011). Steel plate slit damper using on steel frames, Journal of New World Sciences Academy, Engineering Sciences, 6, pp. 1093-1101.

Iwata, M., Kato, T., and Wada, A., (2003).Performance evaluation of buckling-restrained braces in damage-controlled structures. In: Behavior of steel structures in seismic areas: STESSA 2003, pp. 37-43.

Sabelli, R., Mahin, S., Chang, C. (2003). Seismic demands on steel braced frame buildings with buckling-restrained braces, Engineering Structure, 25(5): 655-666.

Iwata, M., and Murai, M. (2006). Buckling-restrained brace using steel mortar planks; performance evaluation as a hysteretic damper. Earthq Eng Struct Dyn, 35(14): 1807-1826.

Tremblay, R., Bolduc, P., Neville, R., and Devall, R. (2006). Seismic testing and performance of buckling-restrained bracing systems. Canad J Civil Eng, 33(2): 183-198.

Benavent Climent A, Oh SH, Akiyama H. (1998). Ultimate energy absorption capacity of slit-type steel plates subjected to shear deformations. J Struct Constr Eng. 503(1): 139-145.

Lee, M.H., Oh, S.H., Huh, C., Oh, Y.S., Yoon, M.H., Moon, T.S. (2002). Ultimate energy absorption capacity of steel plate slit dampers subjected to shear force. Steel Struct. 2(2): 71-79.

Benavent Climent A. (2006). Influence of hysteretic dampers on the seismic response of reinforced concrete wide beam-column connections. Eng Struct. 28(4): 580-592.

Chan, R.W.K., and Albermani, F. (2008). Experimental study of steel slit damper for passive energy dissipation. Eng Struct. 30(4): 1058-1066.

Koetake, Y., Chusilp, P., Zhang, Z., Masakazu, A., Suita, K., Inoue, K., Uno, N. (2005). Mechanical property of beam-to-column moment connection with hysteretic dampers for column weak axis. Eng Struct. 27(1): 109-117.

Oh, S.H., Kim, Y.J., Ryu, H.S., Kang, C.H. (2006). Hysteretic characteristics of beam-to-column connections with energy absorption elements at beam bottom flanges. J Archit Inst Korea Struct Constr, 22(8): 101-108.

Inoue K, Suita K, Takeuchi I, Chusilp P, Nakashima M, Zhou F. (2006). Seismic-resistant weld-free steel frame buildings with mechanical joints and hysteretic dampers. J Struct Eng. 132(6): 864-872.

Tagawa, H., Yamanishi, T., Takaki, A., and Chan, R., (2016). Cyclic behavior of seesaw energy dissipation system with steel slit dampers, Journal of Constructional Steel Research, 117, 24-34.

Hedayat, A.A., (2015).Prediction of the force displacement capacity boundary of an unbuckled steel slit damper. Journal of Constructional Steel Research, 114, pp. 30-50.

Ahmadie Amiri, H., Pournamazian Najafabadi, E., and Estekanchi, H.E., (2018). Experimental and analytical study of Block Slit Damper, Journal of Constructional Steel Research, 141, 167-178.

Oh, S.H., Kim, Y.J., and Ryu, H.S., (2009). Seismic performance of steel structures with slit dampers. Engineering Structures, 31(9), pp. 1997-2008.

Kiani, B.K, Hosseini Hashemi, B., and Torabian, S., (2020). Optimization of slit dampers to improve energy dissipation capacity and low-cycle-fatigue performance, Engineering Structures, 214, ISSN 0141-0296.

Saffari, H., Hedayat, A.A., and PoorsadeghiNejad, M., (2013). Post-Northridge connections with slit dampers to enhance strength and ductility. Journal of Constructional Steel Research, 80, pp. 138-152.

Okada, K., Oh, S.H., Yamada, S., Imaeda, T., Yamaguchi, M., Wada, A. (2001). Experimental study on deformation capacity of composite beams with conventional-type beam-to-column connections. J Struct Constr Eng. 547(9): 161-168.

Engelhardt, M.D., Sabol, T.A. (1998). Reinforcing of steel moment connections with cover plates: Benefits and limitations. Eng Struct. 20(4-6): 510520.

Uang, C.M., and Bondad, D. (1998). Cyclic performance of haunch repaired steel moment connections: Experimental testing and analytical modeling. Eng Struct. 20(4-6): 552-561.